



# An integral equation method for the simulation of doubly-periodic suspensions of rigid bodies in a shearing viscous flow

Jun Wang<sup>a,\*</sup>, Ehssan Nazockdast<sup>b</sup>, Alex Barnett<sup>a</sup>

<sup>a</sup> Flatiron Institute, Simons Foundation, New York, NY 10010, United States of America

<sup>b</sup> The University of North Carolina at Chapel Hill, Chapel Hill, NC 27599, United States of America



## ARTICLE INFO

### Article history:

Received 27 December 2019

Received in revised form 24 August 2020

Accepted 30 August 2020

Available online 3 September 2020

### Keywords:

Stokes flow

Boundary integral equation

Periodic

Rheology

Generalized Greens function

Quadrature

## ABSTRACT

With rheology applications in mind, we present a fast solver for the time-dependent effective viscosity of an infinite lattice containing one or more neutrally buoyant smooth rigid particles per unit cell, in a two-dimensional Stokes fluid with given shear rate. At each time, the mobility problem is reformulated as a 2nd-kind boundary integral equation, then discretized to spectral accuracy by the Nyström method and solved iteratively, giving typically 10 digits of accuracy. Its solution controls the evolution of particle locations and angles in a first-order system of ordinary differential equations. The formulation is placed on a rigorous footing by defining a generalized periodic Green's function for the skew lattice. Numerically, the periodized integral operator is split into a near image sum—applied in linear time via the fast multipole method—plus a correction field solved cheaply via proxy Stokeslets. We use barycentric quadratures to evaluate particle interactions and velocity fields accurately, even at distances much closer than the node spacing. Using first-order time-stepping we simulate, for example, 25 ellipses per unit cell to 3-digit accuracy on a desktop in 1 hour per shear time. Our examples show equilibration at long times, force chains, and two types of blow-ups (jamming) whose power laws match lubrication theory asymptotics.

© 2020 Elsevier Inc. All rights reserved.

## 1. Introduction

Flowing suspensions are ubiquitous in nature and industry, and have been used as model systems for theoretical studies of soft materials. They exhibit complex nonlinear rheological behavior, including shear-thinning, shear-thickening and existence of normal stress differences [19]. Previous theoretical [8,33], computational [31,40,43] and experimental studies [16,9,46,20] have established the prevalence of near-contacts in shear flows, and that near-contact hydrodynamic (lubrication) forces/stresses are key to determining the nonlinear rheology of suspensions, including their shear thickening behavior [5,30,25]. Accurate modeling of flow near such particles is also crucial to understanding transport phenomena such as super-diffusion [41].

Although previous studies have largely focused on spheres, many applications involve suspensions of non-spherical particles [32, Ch. 5]. Moreover, experimental studies show that the rheology of concentrated suspensions, most notably their

\* Corresponding author.

E-mail addresses: [jwang@flatironinstitute.org](mailto:jwang@flatironinstitute.org) (J. Wang), [ehssan@email.unc.edu](mailto:ehssan@email.unc.edu) (E. Nazockdast), [abarnett@flatironinstitute.org](mailto:abarnett@flatironinstitute.org) (A. Barnett).

shear thickening behavior, are highly sensitive to their shape [13,11]. For example, experiments on suspensions of cubic particles show that the viscosity diverges at volume fractions slightly below that of spherical particles, yet the divergence of viscosity and normal stress differences with volume fraction is stronger than those reported for spherical particles [11].

Currently, there is no numerical method that can accurately simulate lubrication forces and stresses in particulate suspensions of complex shape in the Stokes (zero Reynolds number) and non-Brownian (infinite Peclet number) regime. The method that comes closest for *spherical* suspensions is *Stokesian Dynamics* (SD) [12,7,15,43]. In that method, hydrodynamic interactions (HI) are divided into far-field and near-field. The far-field mobility tensor is constructed through a multipole expansion truncated at the stresslet level; the near-field resistance tensor is assumed to be pair-wise additive, and is computed by asymptotic lubrication solutions between two spheres. Despite its huge success, SD cannot be readily used to simulate non-spherical particles, especially their near-field HIs.

In this work, by contrast, we present a convergent numerical method to solve the underlying Stokes mobility boundary value problem (BVP) for arbitrary smooth particle shapes. We use potential theory to reformulate this BVP as a boundary integral equation (BIE) for an unknown Stokeslet “density” on particle boundaries. This BIE approach, which requires the suspending fluid to be Newtonian, has several advantages over conventional discretization (e.g., finite elements): i) since only the boundaries must be discretized there is a large reduction in  $N$ , the number of unknowns; ii) meshing becomes much simpler; iii) unlike with volume discretization, well-conditioned formulations are possible; and iv) close-touching surfaces may be handled without introducing a high density of small volume elements (as in [21]). A possible disadvantage is the loss of sparsity in the resulting linear system; however, algorithms such as the fast multipole method (FMM) [18] are available to apply the dense system matrix in  $\mathcal{O}(N)$  time, leading to optimal-complexity schemes.

Our BIE formulation is a doubly-periodic version of the single-layer formulation of Karrila–Kim [26]; also see Rach–Greengard [38]. Rather than the usual exterior velocity conditions, “interior” traction conditions are imposed, resulting in a 2nd-kind square system with the advantage of hypersingular-free exterior traction evaluations. The motivation to address the periodic case is two-fold: there is interest in i) the rheology of *regular* arrays of rigid particles, with prior numerical [34] and asymptotic analysis work on discs in 2D and spheres in 3D [6]; and ii) the behavior of *random* suspensions via numerical simulation of a finite-sized representative volume element (RVE), where periodic boundary conditions most closely model an infinite system [21,15]. In both cases this is a *homogenization* problem, and the (time-dependent) effective viscosity is sought. Numerically, this demands fast application of a *periodized* integral operator in an arbitrary skewing lattice, for which we simplify and extend the recent method of Barnett, Marple, Veerapaneni, and Zhao [2]. This method (an extension of ideas of Larson–Higdon [28]) splits the periodized kernel into a free-space Stokes FMM sum over nearby images, plus a correction flow that solves an “empty” BVP with smooth data that is solved cheaply using particular solutions. This applies physical periodicity conditions, avoids ad-hoc non-convergent lattice sums [17], and, unlike particle-mesh Ewald (PME) methods which rely on FFTs [1], is spatially adaptive.

This work includes three other innovations. 1) We extend barycentric quadratures for spectrally accurate near-boundary evaluation of the single-layer potential [3] to include the traction needed in our formulation. This allows accurate solutions for inter-particle distances as small as  $d = \mathcal{O}(h^2)$ , where  $h$  is the on-surface node spacing (see Figs. 5–6). 2) We present an efficient way to extract the effective viscosity from the simulation via a line integral (see (14) and section 6.4). 3) We place the entire scheme on a rigorous mathematical footing, proving that the periodized BIE is equivalent to the periodic mobility BVP, by introducing a generalized periodic Stokes Green’s function (section 4.2). As a byproduct we prove existence and uniqueness for the BVP itself (Lemma 4 and Theorem 18).

**Remark 1.** We study the case of pure HIs, which is an accurate physical model for smooth non-Brownian particles not in contact. Previous simulations of spheres in Stokes flow show that HIs alone are not sufficient for preventing particles from making contact and jamming at finite strains [31]. For numerical tractability, non-hydrodynamic forces can be added, either via short-range repulsive forces [40] or collision-free constraint methods [29,47], when particles get closer than a cutoff distance. In experimental settings these new near-contact interactions can, for example, be induced by surface roughness [24,25]. In both experiments and simulations the presence of these non-hydrodynamic near-contact interactions break the fore-aft symmetry of the linear Stokes equation, leading to anisotropy in microstructure and nonlinear rheology [16,8]. Although we do not add such non-hydrodynamic forces, the high accuracy of our quasi-static solver and small time-steps allows converged simulations out to large times without particle collisions when the volume fraction is moderate.

The paper is organized as follows. In section 2, we set up the problem geometry. In section 3, we describe the quasi-static BVP and review its mathematical properties. In section 4, we define a generalized periodic Stokes Green’s function, prove its uniqueness and existence in a constructive manner, and use it to generalize classical potential theory to our periodic case. This section is more mathematical in nature, and application-driven readers can skip some lemmas and proofs as long as the method of construction is understood. In section 5, we reformulate the BVP as a boundary integral equation whose kernel is the periodic Green’s function. In section 6, we give a complete numerical algorithm to solve the quasi-static BVP, followed by a short discussion of time stepping methods in section 7. Numerical examples for both the quasi-static and time dependent problems are given in section 8, including two types of simple jamming behavior. We finish with conclusions in section 9. Two appendices contain technical proofs needed for existence of the periodic Green’s function.

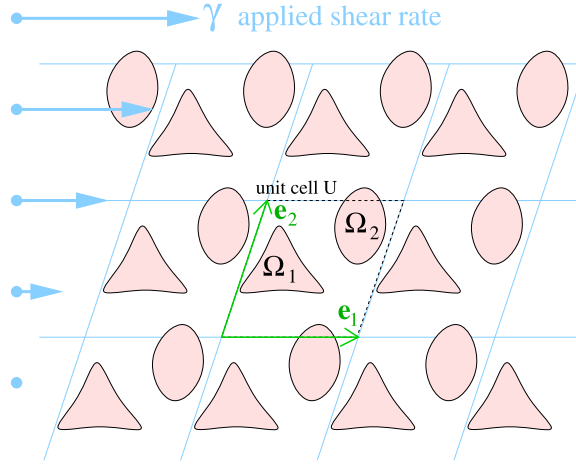


**Fig. 1.** Illustration of the periodic effective viscosity problem. A given shear rate  $\gamma$  is applied to a suspension in a viscous Newtonian background fluid of an infinite lattice of one or more rigid, smooth, neutrally buoyant particles per unit cell (shown is the case of two per unit cell). The suspending fluid has no-slip boundary conditions on each particle. There are no Brownian or contact friction effects.

### 2. Geometry and setup

We first need some geometry notation; see Fig. 1. At any fixed time  $t$ , let  $\mathbf{e}_1$  and  $\mathbf{e}_2$  be two linearly independent vectors that define an infinite lattice in  $\mathbb{R}^2$ . Fixing an arbitrary center, they define a single unit cell  $\mathcal{U}$ , with four walls comprising its boundary  $\partial\mathcal{U} = L \cup R \cup U \cup D$ . We assume that, at this time  $t$ , in the unit cell  $\mathcal{U}$  there are a collection of  $N_o$  disjoint bounded smooth rigid objects  $\{\Omega_j\}_{j=1}^{N_o}$ , with boundaries  $\Gamma_j = \partial\Omega_j$ . Let  $\Omega_\Lambda = \{\mathbf{x} \in \mathbb{R}^2 : \mathbf{x} + m_1\mathbf{e}_1 + m_2\mathbf{e}_2 \in \Omega_j, m_1, m_2 \in \mathbb{Z}, j = 1, \dots, N_o\}$  be the infinite lattice of objects. The centroid of the object  $\Omega_j$  will be  $\mathbf{x}_j^c = \frac{1}{|\partial\Omega_j|} \int_{\partial\Omega_j} \mathbf{x} ds_{\mathbf{x}}$ . An applied shear rate prescribes the change of the lattice with time. For convenience we fix  $\mathbf{e}_1 = (1, 0)$ , but set  $\mathbf{e}_2 = (\gamma t, 1)$  for small times  $t$  (see Section 7), so that the shear rate is the constant  $\gamma$ .<sup>1</sup> When explicit  $t$ -dependence is needed, we will write  $\mathbf{e}_j(t)$ , etc.

We further introduce some notations to describe the rigid body motion. Let  $\mathbf{x}_j^*(0)$  be an arbitrary point on  $\Omega_j(0)$  that is distinct from  $\mathbf{x}_j^c(0)$ . They define a vector  $\mathbf{r}_j(0) = \mathbf{x}_j^*(0) - \mathbf{x}_j^c(0)$ . At a later time  $t$ , they are located at  $\mathbf{x}_j^*$  and  $\mathbf{x}_j^c$ , and the vector they define is  $\mathbf{r}_j(t) = \mathbf{x}_j^*(t) - \mathbf{x}_j^c(t)$ . We define the angular position  $\theta_j(t)$  to be the angle from  $\mathbf{r}_j(0)$  to  $\mathbf{r}_j(t)$ . Since a rigid body motion is assumed,  $\theta_j(t)$  is independent of the choice of  $\mathbf{x}_j^*$  and  $\mathbf{x}_j^c$ . The linear velocity is defined as  $\mathbf{v}_j = \frac{d}{dt}\mathbf{x}_j^c(t)$  and the angular velocity is defined as  $\omega_j = \frac{d}{dt}\theta_j(t)$ .

For this problem, we have as input the initial configuration of the objects defined by  $\{\Omega_j(0)\}_{j=1}^{N_o}$ ,  $\{\mathbf{x}_j^c(0)\}_{j=1}^{N_o}$  and  $\{\theta_j(0)\}_{j=1}^{N_o}$ , the unit cell defined by  $\{\mathbf{e}_1(0), \mathbf{e}_2(0)\}$ , and the background flow with shear rate  $\gamma$  and viscosity  $\mu$ . We are interested in studying the evolution of such a system. More specifically, we seek solutions of the following quantities: the velocity field of the fluid  $\mathbf{u} = \mathbf{u}(\mathbf{x}, t)$ , the pressure field  $p = p(\mathbf{x}, t)$ , the motion of the objects  $\{\mathbf{x}_j^c(t), \theta_j(t)\}_{j=1}^{N_o}$ , and macroscopic derived quantities such as the effective viscosity defined later by (14).

A list of notations for the main objects in this paper is given in Table 1. Most of them are standard for Stokes flows. We also adopt MATLAB-style notation for block vectors and matrices throughout this paper, using commas to indicate horizontal stacking and semicolons to indicate vertical stacking. For example,  $\mathbf{g} = [\mathbf{g}_1; \mathbf{g}_2; \mathbf{g}_3; \mathbf{g}_4]$  means that  $\mathbf{g}$  is formed by stacking the vectors  $\mathbf{g}_1, \dots, \mathbf{g}_4$  vertically. When a tensor (e.g.  $\mathbf{G}$ ) is contracted with a vector (e.g.  $\mathbf{f}$ ) we denote the resulting vector by  $\mathbf{G}\mathbf{f}$  or  $\mathbf{G} \cdot \mathbf{f}$ . Vector inner products are denoted  $\mathbf{g} \cdot \mathbf{f}$  or  $(\mathbf{g}, \mathbf{f})$ .

### 3. The quasi-static mobility boundary value problem

Since we are in the viscous regime, there is no inertia, and the particle velocities  $\{\mathbf{v}_j(t), \omega_j(t)\}_{j=1}^{N_o}$  are determined entirely by their current locations  $\{\mathbf{x}_j^c(t), \theta_j(t)\}_{j=1}^{N_o}$ , via solving a quasi-static *mobility* problem with zero applied forces and torques. To phrase this as a BVP we need some basic definitions in Stokes flows. We let  $\mathbf{u}(\mathbf{x}) = (u_1(\mathbf{x}), u_2(\mathbf{x}))$  be the fluid velocity and  $p(\mathbf{x})$  be the pressure in the suspending fluid  $\mathbb{R}^2 \setminus \overline{\Omega_\Lambda}$ , and let  $\boldsymbol{\sigma}$  be the stress tensor associated with a function pair  $(\mathbf{u}, p)$ :

$$\boldsymbol{\sigma}_{ij}(\mathbf{u}, p) = -\delta_{ij}p + \mu \left( \frac{\partial u_i}{\partial x_j} + \frac{\partial u_j}{\partial x_i} \right) = -\delta_{ij}p + \mu e(\mathbf{u}), \quad i, j = 1, 2, \tag{1}$$

<sup>1</sup> Often the shear rate is denoted by  $\dot{\gamma}$ ; for simplicity we drop the dot.

**Table 1**  
Table of main symbols used in this work.

Symbol	Type	Meaning
$\mu, \mu^{\text{eff}}$	scalar	viscosity
$\mathbf{u}, \mathbf{v}, \mathbf{w}$	vector field	fluid velocity
$w_j$	scalar	angular velocity of $j$ th body $\Omega_j$
$\mathbf{x}_j^c, \mathbf{v}_j$	vectors	position, velocity of centroid of $\Omega_j$
$p, q, r$	scalar field	fluid pressure
$\boldsymbol{\sigma}$	tensor field	fluid stress
$\mathbf{T}$	vector (defined on surface)	traction
$\boldsymbol{\rho}$	vector (defined on surface)	single-layer (force) density
$\mathbf{G}(\mathbf{x}, \mathbf{y}), \mathbf{G}_{\text{per}}(\mathbf{x}, \mathbf{y})$	tensor kernel	Stokeslet (single-layer kernel)
$\mathbf{G}^p(\mathbf{x}, \mathbf{y}), \mathbf{G}_{\text{per}}^p(\mathbf{x}, \mathbf{y})$	vector kernel	single-layer pressure kernel
$\mathbf{G}^t(\mathbf{x}, \mathbf{y}), \mathbf{G}_{\text{per}}^t(\mathbf{x}, \mathbf{y})$	tensor kernel	single-layer traction kernel
$\mathcal{U}$	planar domain	unit cell with walls $L, R, D, U$

where  $\delta_{ij}$  is the Kronecker delta. Here  $e(\mathbf{u}) := \frac{1}{2}(D\mathbf{u} + D\mathbf{u}^T)$  is the strain tensor, where  $D\mathbf{u} := \begin{bmatrix} \frac{\partial u_1}{\partial x_1} & \frac{\partial u_1}{\partial x_2} \\ \frac{\partial u_2}{\partial x_1} & \frac{\partial u_2}{\partial x_2} \end{bmatrix}$  is the gradient of the velocity.

The surface hydrodynamic traction  $\mathbf{T}(\mathbf{u}, p)$  (force vector per unit length that a boundary with outward unit normal vector  $\mathbf{n}$  applies to the fluid) is given by:

$$\mathbf{T}(\mathbf{u}, p) = \boldsymbol{\sigma} \cdot \mathbf{n} = \begin{bmatrix} \sigma_{11} & \sigma_{12} \\ \sigma_{21} & \sigma_{22} \end{bmatrix} \begin{bmatrix} n_1 \\ n_2 \end{bmatrix}. \quad (2)$$

For notational convenience, we also define  $\mathbf{x}^\perp = \begin{bmatrix} -x_2 \\ x_1 \end{bmatrix}$  and  $\nabla^\perp = \begin{bmatrix} -\frac{\partial}{\partial x_2} \\ \frac{\partial}{\partial x_1} \end{bmatrix}$ .

We seek solutions  $(\mathbf{u}, p)$  and  $\{(\mathbf{v}_i, \omega_i)\}_{i=1}^{N_o}$  to the following quasi-static BVP:

$$-\mu \Delta \mathbf{u} + \nabla p = \mathbf{0} \quad (\mathbf{x} \in \mathbb{R}^2 \setminus \overline{\Omega_\Lambda}) \quad (3)$$

$$\nabla \cdot \mathbf{u} = 0 \quad (\mathbf{x} \in \mathbb{R}^2 \setminus \overline{\Omega_\Lambda}) \quad (4)$$

$$\mathbf{u}(\mathbf{x}) + \mathbf{u}_0(\mathbf{x}) = \mathbf{v}_i + \omega_i (\mathbf{x} - \mathbf{x}_i^c)^\perp \quad (\mathbf{x} \in \Gamma_i, i = 1, \dots, N_o) \quad (5)$$

$$\int_{\Gamma_i} \mathbf{T}(\mathbf{u}, p) ds_{\mathbf{x}} = \mathbf{0} \quad (6)$$

$$\int_{\Gamma_i} (\mathbf{T}(\mathbf{u}, p), (\mathbf{x} - \mathbf{x}_i^c)^\perp) ds_{\mathbf{x}} = 0 \quad (7)$$

$$\mathbf{u}(\mathbf{x} + m_1 \mathbf{e}_1 + m_2 \mathbf{e}_2) = \mathbf{u}(\mathbf{x}) \quad (m_1, m_2 \in \mathbb{Z}) \quad (8)$$

$$p(\mathbf{x} + m_1 \mathbf{e}_1 + m_2 \mathbf{e}_2) = p(\mathbf{x}) \quad (m_1, m_2 \in \mathbb{Z}). \quad (9)$$

Here  $(\cdot, \cdot)$  is the Euclidean inner product for vectors in  $\mathbb{R}^2$ .  $\mathbf{u}_0(\mathbf{x}) = \begin{bmatrix} \gamma x_2 \\ 0 \end{bmatrix}$  is the background shear flow with the given lattice shear rate  $\gamma$ , which is a Stokes solution when paired with the pressure field  $p_0 \equiv 0$ . Then  $(\mathbf{u}, p)$  can be viewed as the perturbation of this velocity and pressure field, which, once obtained, can be added to  $(\mathbf{u}_0, p_0)$  to recover the physical velocity and pressure  $\tilde{\mathbf{u}} = \mathbf{u} + \mathbf{u}_0$  and  $\tilde{p} = p + p_0$ . Both  $(\mathbf{u}_0, p_0)$  and  $(\mathbf{u}, p)$  satisfy the governing equations of Stokes flows (3) and (4). Equation (5) enforces rigid body motion of  $\Omega_i$ . Equations (6) and (7) state that the net force and torque (induced by  $(\mathbf{u}, p)$ ) on the boundary  $\Gamma_i$  are zero. It can be verified directly that  $(\mathbf{u}_0, p_0)$  does not contribute to the net force nor torque, i.e.  $\int_{\Gamma_i} \mathbf{T}(\mathbf{u}_0, p_0) ds_{\mathbf{x}} = \mathbf{0}$  and  $\int_{\Gamma_i} (\mathbf{T}(\mathbf{u}_0, p_0), (\mathbf{x} - \mathbf{x}_i^c)^\perp) ds_{\mathbf{x}} = 0$ , which implies that the physical force and torque (induced by  $(\tilde{\mathbf{u}}, \tilde{p})$ ) are also zero. Finally, (8) and (9) enforce lattice periodicity of the solution.

**Remark 2.** The periodicity condition (8) and (9) are equivalent to the unit cell matching conditions

$$\mathbf{u}_R - \mathbf{u}_L = \mathbf{0} \quad (10)$$

$$\mathbf{T}(\mathbf{u}, p)_R - \mathbf{T}(\mathbf{u}, p)_L = \mathbf{0} \quad (11)$$

$$\mathbf{u}_U - \mathbf{u}_D = \mathbf{0} \quad (12)$$

$$\mathbf{T}(\mathbf{u}, p)_U - \mathbf{T}(\mathbf{u}, p)_D = \mathbf{0}, \quad (13)$$

where the notation  $\mathbf{u}_R$  is used to mean the restriction of  $\mathbf{u}$  to the wall  $R$ . It is straightforward to show that equations (8)–(9) imply (10)–(13). The converse follows by the unique continuation of Cauchy data  $(\mathbf{u}, \mathbf{T})$  as a solution to the 2nd-order Stokes PDE.

Once the quasi-static solution  $(\mathbf{u}, p)$  is obtained at a given time  $t$ , the effective viscosity can be retrieved (in the case where no object intersects the bottom wall  $D$ ) by

$$\mu_{\text{eff}}(t) := \frac{1}{\gamma|\mathbf{e}_1|} \int_D \mathbf{t} \cdot \mathbf{T}(\mathbf{u} + \mathbf{u}_0, p) \, ds_{\mathbf{x}}, \tag{14}$$

where  $\mathbf{t} = (1, 0)$  is the unit tangent vector on  $D$ . Its interpretation is simply the total horizontal (shear) force transmitted through the bottom wall by the fluid. This formula bypasses the more complicated extraction of  $\mu_{\text{eff}}(t)$  as a cell average of stress common in chemical engineering [15, Eq. (8)]. In Sec. 6.4 we will present a variant of (14) that is more efficient to evaluate, and which remains valid when particles intersect  $D$ .

We can show that the above BVP has a three-dimensional nullspace, which relies on the following lemma.

**Lemma 3.** *If  $(\mathbf{u}, p)$  satisfies (3)–(9) with  $\mathbf{u}_0 = \mathbf{0}$  (homogeneous case), then*

$$\int_{\Gamma_i} (\mathbf{u}, \mathbf{T}(\mathbf{u}, p)) \, ds_{\mathbf{x}} = 0. \tag{15}$$

**Proof.**

$$\begin{aligned} \int_{\Gamma_i} (\mathbf{u}, \mathbf{T}(\mathbf{u}, p)) \, ds_{\mathbf{x}} &= \int_{\Gamma_i} (\mathbf{v}_i + \omega_i (\mathbf{x} - \mathbf{x}_i^c)^\perp, \mathbf{T}(\mathbf{u}, p)) \, ds_{\mathbf{x}} \\ &= \left( \mathbf{v}_i, \int_{\Gamma_i} \mathbf{T}(\mathbf{u}, p) \, ds_{\mathbf{x}} \right) + \omega_i \int_{\Gamma_i} ((\mathbf{x} - \mathbf{x}_i^c)^\perp, \mathbf{T}(\mathbf{u}, p)) \, ds_{\mathbf{x}} \\ &= (\mathbf{v}_i, \mathbf{0}) + \omega_i \cdot 0 = 0. \quad \square \end{aligned}$$

Combining this with the divergence theorem, we get the following lemma on the uniqueness of the solution to the BVP.

**Lemma 4.** *If  $(\mathbf{u}, p)$  satisfies (3)–(9) with  $\mathbf{u}_0 = \mathbf{0}$ , then  $\mathbf{u}(\mathbf{x}) = \text{const}$ , and  $p(\mathbf{x}) = \text{const}$ .*

**Proof.** Letting  $\langle \cdot, \cdot \rangle : \mathbb{R}^{2 \times 2} \times \mathbb{R}^{2 \times 2}$  be the Frobenius inner product, we have

$$\begin{aligned} \int_{\mathcal{U} \setminus \Omega_\Lambda} \langle e(\mathbf{u}), e(\mathbf{u}) \rangle \, dV &= \int_{\mathcal{U} \setminus \Omega_\Lambda} \langle D\mathbf{u}, e(\mathbf{u}) \rangle \, dV \\ &= \int_{\partial(\mathcal{U} \setminus \Omega_\Lambda)} (\mathbf{u}, e(\mathbf{u}) \cdot \mathbf{n}) \, ds_{\mathbf{x}} - \frac{1}{2} \int_{\mathcal{U} \setminus \Omega_\Lambda} (\mathbf{u}, \Delta \mathbf{u}) \, dV \\ &= \int_{\partial(\mathcal{U} \setminus \Omega_\Lambda)} (\mathbf{u}, e(\mathbf{u}) \cdot \mathbf{n}) \, ds_{\mathbf{x}} - \frac{1}{2\mu} \int_{\mathcal{U} \setminus \Omega_\Lambda} (\mathbf{u}, \nabla p) \, dV \\ &= \frac{1}{2\mu} \int_{\partial(\mathcal{U} \setminus \Omega_\Lambda)} \left( \mathbf{u}, \left( -p \begin{bmatrix} 1 & 0 \\ 0 & 1 \end{bmatrix} + 2\mu e(\mathbf{u}) \right) \cdot \mathbf{n} \right) \, ds_{\mathbf{x}} \\ &= -\frac{1}{2\mu} \sum_{i=1}^{N_o} \int_{\Gamma_i} (\mathbf{u}, \mathbf{T}) \, ds_{\mathbf{x}} + \frac{1}{2\mu} \int_{\partial \mathcal{U}} (\mathbf{u}, \mathbf{T}) \, ds_{\mathbf{x}} \\ &= \frac{1}{2\mu} \int_{\partial \mathcal{U}} (\mathbf{u}, \mathbf{T}) \, ds_{\mathbf{x}} = 0. \end{aligned}$$

The second line follows from Green’s first identity, the fourth line follows from the divergence theorem, and the last line combines the result of Lemma 3 and the periodicity of  $\mathbf{u}$  and  $\mathbf{T}$ .

As a result, we get:

$$e(\mathbf{u}) \equiv \begin{bmatrix} 0 & 0 \\ 0 & 0 \end{bmatrix}, \quad \mathbf{x} \in \mathcal{L} \setminus \Omega_\Lambda. \tag{16}$$

Thus,  $\mathbf{u}$  is a rigid body motion, i.e.  $\mathbf{u}(\mathbf{x}) = \mathbf{v}_0 + \omega_0(\mathbf{x} - \mathbf{x}_0)^\perp$ .

Letting  $\mathbf{x}_L \in L$  and  $\mathbf{x}_R = \mathbf{x}_L + \mathbf{e}_1 \in R$ , we get:

$$\mathbf{u}(\mathbf{x}_L) = \mathbf{v}_0 + \omega_0(\mathbf{x}_L - \mathbf{x}_0)^\perp \tag{17}$$

$$\mathbf{u}(\mathbf{x}_L + \mathbf{e}_1) = \mathbf{v}_0 + \omega_0(\mathbf{x}_L + \mathbf{e}_1 - \mathbf{x}_0)^\perp. \tag{18}$$

Subtracting (18) and (17) and recalling the periodicity in  $\mathbf{u}$  leads to  $\omega_0 \mathbf{e}_1^\perp = 0$ , which means  $\omega_0 = 0$ , and thus  $\mathbf{u}(\mathbf{x}) = \mathbf{v}_0$ . Substituting this into equation (3) yields  $\nabla p = \mathbf{0}$ , which further means  $p = \text{const.}$   $\square$

**Remark 5.** The existence of a solution to the quasi-static BVP comes from that of the integral formulation and will be proved in Section 5.

#### 4. Green's functions and Stokes layer potentials

In this section we review some basic properties of the free space Stokes Green's function and layer potentials, then propose a *generalized* periodic Green's function that exists even in the case of non-zero net force in the unit cell. Its construction, both analytically and numerically, involves a direct sum of only the nearest free-space image sources, plus an auxiliary Stokes solution that corrects for their failure in periodicity. When the net force is zero, as occurs in our application, this Green's function will in fact be periodic.

##### 4.1. The free space Green's function and layer potentials

For convenience we gather some standard potential theory formulae for Stokes in 2D [23, Sec. 2.2, 2.3], following the notation of [2]. The free space Green's function to the Stokes equation (also called Stokeslet or single-layer kernel) is defined to be the tensor  $\mathbf{G}(\mathbf{x}, \mathbf{y})$  with components:

$$\mathbf{G}_{ij}(\mathbf{x}, \mathbf{y}) = \frac{1}{4\pi\mu} \left( \delta_{ij} \log \frac{1}{r} + \frac{r_i r_j}{r^2} \right), \quad i, j = 1, 2, \quad \mathbf{r} := \mathbf{x} - \mathbf{y}, \quad r := \|\mathbf{r}\|, \tag{19}$$

and the single-layer pressure kernel is the vector  $\mathbf{G}^p$  with components

$$\mathbf{G}_j^p(\mathbf{x}, \mathbf{y}) = \frac{1}{2\pi} \frac{r_j}{r^2}, \quad j = 1, 2. \tag{20}$$

We will also need the single-layer traction kernel  $\mathbf{G}^t$  with components

$$\mathbf{G}_{ik}^t(\mathbf{x}, \mathbf{y}) = \sum_{j=1}^2 \sigma_{ij}(\mathbf{G}_{\cdot,k}(\cdot, \mathbf{y}), \mathbf{G}_k^p(\cdot, \mathbf{y}))(\mathbf{x}) \mathbf{n}_j^x = -\frac{1}{\pi} \frac{r_i r_k}{r^2} \frac{\mathbf{r} \cdot \mathbf{n}^x}{r^2}, \quad i, k = 1, 2, \tag{21}$$

where the target  $\mathbf{x}$  is assumed to be on a surface with normal  $\mathbf{n}^x$ .

The Stokeslet allows us to express the velocity field  $\mathbf{u} = (u_1, u_2)$  and pressure field  $p$  induced by a point force  $\mathbf{f} = (f_1, f_2)$  at  $\mathbf{y}_0 = (y_{01}, y_{02})$  as:

$$u_i = \sum_{j=1}^2 \mathbf{G}_{ij}(\mathbf{x}, \mathbf{y}_0) f_j, \quad p = \sum_{j=1}^2 \mathbf{G}_j^p(\mathbf{x}, \mathbf{y}_0) f_j. \tag{22}$$

Let  $\Gamma$  be a smooth closed curve in  $\mathbb{R}^2$  with exterior  $\Omega^+$  and interior  $\Omega^-$ . Let  $\mathbf{n}_{\mathbf{x}_0}$  be the unit outward normal at  $\mathbf{x}_0 \in \Gamma$ . The single layer Stokes potential represents the velocity field  $\mathbf{u}(\mathbf{x})$  and pressure field  $p(\mathbf{x})$  induced by a surface force  $\boldsymbol{\rho}(\mathbf{x}) = (\rho_1(\mathbf{x}), \rho_2(\mathbf{x}))$  on a boundary  $\Gamma$  as:

$$\mathbf{u}(\mathbf{x}) = \mathcal{S}_\Gamma[\boldsymbol{\rho}](\mathbf{x}) = \int_\Gamma \mathbf{G}(\mathbf{x}, \mathbf{y}) \boldsymbol{\rho}(\mathbf{y}) ds_{\mathbf{y}}, \quad p(\mathbf{x}) = \mathcal{S}_\Gamma^p[\boldsymbol{\rho}] = \int_\Gamma \mathbf{G}^p(\mathbf{x}, \mathbf{y}) \boldsymbol{\rho}(\mathbf{y}) ds_{\mathbf{y}}. \tag{23}$$

The associated traction is given by:

$$\mathbf{T}(\mathbf{x}) = \mathcal{S}_\Gamma^t[\boldsymbol{\rho}](\mathbf{x}) = \int_\Gamma \mathbf{G}^t(\mathbf{x}, \mathbf{y}) \boldsymbol{\rho}(\mathbf{y}) ds_{\mathbf{y}}. \tag{24}$$

It is well known in classical potential theory that the single layer potential has the following properties.

**Lemma 6** (jump relation). Let  $\mathbf{u}(\mathbf{x}) = \mathcal{S}_\Gamma[\boldsymbol{\rho}](\mathbf{x})$  and  $\mathbf{T}(\mathbf{x}) = \mathcal{S}_\Gamma^t[\boldsymbol{\rho}](\mathbf{x})$  be the velocity and traction of a single layer potential with density  $\boldsymbol{\rho}$  defined on  $\Gamma$ . Then  $\mathcal{S}_\Gamma \boldsymbol{\rho}(\mathbf{x})$  satisfies the Stokes equations (3) and (4) in  $\mathbb{R}^2 \setminus \Gamma$  and continuous in  $\mathbb{R}^2$ . The single layer traction satisfies the jump relations:

$$\lim_{\substack{\mathbf{x} \rightarrow \mathbf{x}_0 \\ \mathbf{x} \in \Omega^\pm}} \mathbf{T}(\mathbf{x}) = \mp \frac{1}{2} \boldsymbol{\rho}(\mathbf{x}_0) + \oint_{\Gamma} \mathbf{G}^t(\mathbf{x}_0, \mathbf{y}) \boldsymbol{\rho}(\mathbf{y}) ds_{\mathbf{y}}, \tag{25}$$

where  $\oint_{\Gamma}$  indicates the principal value integral over the curve  $\Gamma$ .

**Lemma 7.** Let  $\mathbf{u}(\mathbf{x}) = \mathcal{S}_\Gamma[\boldsymbol{\rho}](\mathbf{x})$  and  $\mathbf{T}(\mathbf{x}) = \mathcal{S}_\Gamma^t[\boldsymbol{\rho}](\mathbf{x})$  be the velocity and traction of a single layer potential with density  $\boldsymbol{\rho}$  defined on  $\Gamma$ . Let  $\mathbf{T}_-$  and  $\mathbf{T}_+$  denote the limits of the traction from the interior and exterior respectively. We have the following:

$$\int_{\Gamma} \mathbf{T}_+ ds_{\mathbf{x}} = - \int_{\Gamma} \boldsymbol{\rho}(\mathbf{x}) ds_{\mathbf{x}}, \quad \int_{\Gamma} \mathbf{T}_- ds_{\mathbf{x}} = \mathbf{0}, \tag{26}$$

and

$$\int_{\Gamma} \left( (\mathbf{x} - \mathbf{x}^c)^\perp, \mathbf{T} \right)_+ ds_{\mathbf{x}} = - \int_{\Gamma} \left( (\mathbf{x} - \mathbf{x}^c)^\perp, \boldsymbol{\rho} \right) ds_{\mathbf{x}}, \tag{27}$$

$$\int_{\Gamma} \left( (\mathbf{x} - \mathbf{x}^c)^\perp, \mathbf{T} \right)_- ds_{\mathbf{x}} = 0, \tag{28}$$

and

$$\int_{\Gamma} \mathbf{u} \cdot \mathbf{n} ds_{\mathbf{x}} = 0, \tag{29}$$

which can be interpreted as the net force, torque and flux respectively.

#### 4.2. A generalized periodic Stokes Green's function

We now must generalize the concept of a periodic Green's function, since a single Stokeslet source (having non-zero net force) cannot be periodized. This fact is analogous to the non-existence of a domain Green's function for the interior Laplace Neumann problem; yet, in that setting there is a ‘‘Neumann function’’ [27] which, when applied to zero-mean data, recovers a solution obeying the Neumann boundary conditions. Our generalized Green's function is analogous to this Neumann function: it distributes the net force in a prescribed fashion on the boundary, so that when the net force is non-zero, the traction is not periodic across unit cell walls (Remark 13). One motivation is the rigorous analysis in this paper; another is to numerically handle non-zero net force case in a predictable, linear way, for stability in the iterative solver.

**Definition 8.** Let  $\mathcal{U}$  be a unit cell with four walls comprising its boundary  $\partial\mathcal{U} = L \cup R \cup U \cup D$ . For each source point  $\mathbf{y} \in \mathcal{U}$ , and each force vector  $\mathbf{f}$ , let the pair  $(\mathbf{w}_{\mathbf{y},\mathbf{f}}(\mathbf{x}), q_{\mathbf{y},\mathbf{f}}(\mathbf{x}))$  be the solution of the Stokes BVP:

$$-\mu \Delta \mathbf{w} + \nabla q = \mathbf{f} \delta_{\mathbf{y}} \quad \text{in } \mathcal{U} \tag{30}$$

$$\nabla \cdot \mathbf{w} = 0 \quad \text{in } \mathcal{U} \tag{31}$$

$$\mathbf{w}_R - \mathbf{w}_L = \mathbf{0} \tag{32}$$

$$\mathbf{T}(\mathbf{w}, q)_R - \mathbf{T}(\mathbf{w}, q)_L = \mathbf{f}/2|\mathbf{e}_2| \tag{33}$$

$$\mathbf{w}_U - \mathbf{w}_D = \mathbf{0} \tag{34}$$

$$\mathbf{T}(\mathbf{w}, q)_U - \mathbf{T}(\mathbf{w}, q)_D = \mathbf{f}/2|\mathbf{e}_1|. \tag{35}$$

Here  $\mathbf{e}_1$  and  $\mathbf{e}_2$  are the unit cell lattice vectors, and  $\delta_{\mathbf{y}}$  is the delta function centered at  $\mathbf{y}$ . Considering two specific choices of the force  $\mathbf{f} = (1, 0)$  and  $\mathbf{f} = (0, 1)$ , the generalized periodic Green's function, as a function of  $\mathbf{x} \in \mathcal{U}$ , is defined as  $\mathbf{G}_{per}(\mathbf{x}, \mathbf{y}) := [\mathbf{w}_{\mathbf{y},(1,0)}(\mathbf{x}), \mathbf{w}_{\mathbf{y},(0,1)}(\mathbf{x})]$ . Its associated pressure and traction kernels are similarly defined:

$$\mathbf{G}_{per}^p(\mathbf{x}, \mathbf{y}) := [q_{\mathbf{y},(1,0)}(\mathbf{x}); q_{\mathbf{y},(0,1)}(\mathbf{x})] \tag{36}$$

$$\mathbf{G}_{per}^t(\mathbf{x}, \mathbf{y}) := [\mathbf{T}(\mathbf{w}_{(1,0)}, q_{\mathbf{y},(1,0)})(\mathbf{x}), \mathbf{T}(\mathbf{w}_{\mathbf{y},(0,1)}, q_{\mathbf{y},(0,1)})(\mathbf{x})]. \tag{37}$$

We will prove later in this section that this generalized periodic Green's function  $\mathbf{G}_{per}$  is determined only up to a constant  $\mathbf{c} \in \mathbb{R}^2$ . Similarly  $\mathbf{G}_{per}^p$  is determined up to a constant  $c$  and  $\mathbf{G}_{per}^t$  is determined up to a constant  $\mathbf{cn}_x$ .  $\mathbf{G}_{per}$  is a smooth perturbation of  $\mathbf{G}$ , and the difference can be found by solving the following subproblem that we call the ‘‘empty BVP.’’ This is a periodic version of the construction of the domain Green's function in classical PDE theory [14, Sec. 7.H].

For a given discrepancy vector  $\mathbf{g} = [\mathbf{g}_1; \mathbf{g}_2; \mathbf{g}_3; \mathbf{g}_4]$ , the empty BVP (EBVP) seeks a function pair  $(\mathbf{v}, q)$  solving:

$$-\mu \Delta \mathbf{v} + \nabla q = \mathbf{0} \quad \text{in } \mathcal{U} \tag{38}$$

$$\nabla \cdot \mathbf{v} = 0 \quad \text{in } \mathcal{U} \tag{39}$$

$$\mathbf{v}_R - \mathbf{v}_L = \mathbf{g}_1 \tag{40}$$

$$\mathbf{T}(\mathbf{v}, q)_R - \mathbf{T}(\mathbf{v}, q)_L = \mathbf{g}_2 \tag{41}$$

$$\mathbf{v}_U - \mathbf{v}_D = \mathbf{g}_3 \tag{42}$$

$$\mathbf{T}(\mathbf{v}, q)_U - \mathbf{T}(\mathbf{v}, q)_D = \mathbf{g}_4. \tag{43}$$

We now extend the consistency and uniqueness of the EBVP given in [2, Prop. 4.2] to include existence, which was not proven in that work. We are interested in smooth solutions, which requires a technical condition that  $\mathbf{g}$  is generated from a smooth flow and pressure function pair  $(\mathbf{w}, r)$ . Note that  $(\mathbf{w}, r)$  need not satisfy the Stokes equations, and  $\mathbf{w}$  need not even be divergence-free. Its proof is in Appendix A.

**Theorem 9.** *Let the discrepancy data  $\mathbf{g} = [\mathbf{g}_1; \mathbf{g}_2; \mathbf{g}_3; \mathbf{g}_4]$  be smooth in the sense that it is extracted as follows from a  $C^\infty(\bar{\mathcal{U}})$  smooth function pair  $(\mathbf{w}, r)$ :*

$$\mathbf{g}_1 = \mathbf{w}_R - \mathbf{w}_L \tag{44}$$

$$\mathbf{g}_2 = \mathbf{T}(\mathbf{w}, r)_R - \mathbf{T}(\mathbf{w}, r)_L \tag{45}$$

$$\mathbf{g}_3 = \mathbf{w}_U - \mathbf{w}_D \tag{46}$$

$$\mathbf{g}_4 = \mathbf{T}(\mathbf{w}, r)_U - \mathbf{T}(\mathbf{w}, r)_D. \tag{47}$$

Let  $\mathbf{g}$  also be consistent in the sense that three scalar conditions hold:

$$\int_L \mathbf{g}_2 ds + \int_D \mathbf{g}_4 ds = \mathbf{0} \quad (\text{zero net force}), \text{ and} \tag{48}$$

$$\int_L \mathbf{n} \cdot \mathbf{g}_1 ds + \int_D \mathbf{n} \cdot \mathbf{g}_3 ds = 0 \quad (\text{volume conservation}). \tag{49}$$

Then there exists a  $C^\infty(\mathcal{U})$  solution  $(\mathbf{v}, q)$  to the EBVP (38)–(43), and its nullity is 3. Specifically, the solution is unique up to translational flow and additive pressure constants, with solution space  $(\mathbf{v} + \mathbf{c}, q + c)$ , for  $(\mathbf{c}, c) \in \mathbb{R}^3$ .

Utilizing the solution to this subproblem as a building block, we now proceed to construct the periodic Green's function, or equivalently, the solution of the BVP (30)–(35) for a given point force  $\mathbf{f} = (f_1, f_2)$  at  $\mathbf{y} = (y_1, y_2)$ . We begin by defining a nearby image source sum, then a metric of the failure to be periodic.

**Definition 10.** Let  $\mathbf{y} \in \mathcal{U}$  be a point in the unit cell, and  $\mathbf{f} \in \mathbb{R}^2$  be an arbitrary vector. Let  $\tilde{\mathcal{U}}$  be the expanded unit cell with the same center and walls parallel to that of the original cell about twice their length (as is illustrated in Fig. 2).  $\mathbf{w}^{near}$  and  $q^{near}$  are defined to be the sum of neighboring copies of the free space Stokeslets that are inside  $\tilde{\mathcal{U}}$ , i.e.

$$\mathbf{w}^{near}(\mathbf{x}) = \mathbf{G}_{near}(\mathbf{x}, \mathbf{y})\mathbf{f} := \sum_{m, n \in \mathbb{Z}: \mathbf{y} + m\mathbf{e}_1 + n\mathbf{e}_2 \in \tilde{\mathcal{U}}} \mathbf{G}(\mathbf{x}, \mathbf{y} + m\mathbf{e}_1 + n\mathbf{e}_2)\mathbf{f} \tag{50}$$

$$q^{near}(\mathbf{x}) = \mathbf{G}_{near}^p(\mathbf{x}, \mathbf{y}) \cdot \mathbf{f} := \sum_{m, n \in \mathbb{Z}: \mathbf{y} + m\mathbf{e}_1 + n\mathbf{e}_2 \in \tilde{\mathcal{U}}} \mathbf{G}^p(\mathbf{x}, \mathbf{y} + m\mathbf{e}_1 + n\mathbf{e}_2) \cdot \mathbf{f}. \tag{51}$$

**Definition 11.** Let  $\tilde{\mathcal{U}}$ ,  $\mathbf{y}$  and  $\mathbf{f}$  be the same as in Definition 10.  $w^{corr}$  and  $q^{corr}$  are defined to be the solution to the empty box BVP (38)–(43), with the ‘‘discrepancy vector’’  $\mathbf{g} = [\mathbf{g}_1; \mathbf{g}_2; \mathbf{g}_3; \mathbf{g}_4]$  as follows:

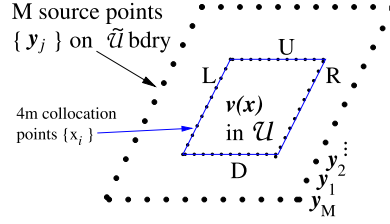


Fig. 2. Illustration of the solution method for the “empty box” BVP which is used to correct the deviation from periodicity in the near image sum.

$$\mathbf{g}_1 = -(\mathbf{w}_R^{near} - \mathbf{w}_L^{near}) \tag{52}$$

$$\mathbf{g}_2 = -(\mathbf{T}_R^{near} - \mathbf{T}_L^{near}) + \mathbf{f}/2|\mathbf{e}_2| \tag{53}$$

$$\mathbf{g}_3 = -(\mathbf{w}_U^{near} - \mathbf{w}_D^{near}) \tag{54}$$

$$\mathbf{g}_4 = -(\mathbf{T}_U^{near} - \mathbf{T}_D^{near}) + \mathbf{f}/2|\mathbf{e}_1|. \tag{55}$$

We now claim that the specific choice of  $\mathbf{g}$  just defined leads to existence of an EBVP solution  $(\mathbf{v}, q)$ . The following is proved in Appendix B.

**Theorem 12.** *Let the discrepancy vector  $\mathbf{g} = [\mathbf{g}_1; \mathbf{g}_2; \mathbf{g}_3; \mathbf{g}_4]$  be given by (52)–(55). Then a solution  $(\mathbf{v}, q)$  to the EBVP (38)–(43) exists and is unique up to additive constants in  $\mathbf{v}$  and  $q$ .*

Note that the inclusion of all the image sources lying in an dilation of the unit cell in  $\mathbf{w}^{near}$  and  $q^{near}$  from Definition 10 actually results in cancellations of all nearby source contributions to the discrepancy  $\mathbf{g}$ ; see [2]. This results in  $\mathbf{g}$  being smooth, so that the numerical solution of the empty BVP (section 6.1) will be rapidly convergent, needing only  $\mathcal{O}(1)$  effort.

It is trivial to observe that both the “near part”  $(\mathbf{w}^{near}, q^{near})$  and the “correction part”  $(\mathbf{w}^{corr}, q^{corr})$  satisfy equations (30)–(31), and that the discrepancy (52)–(53) of  $(\mathbf{w}^{corr}, q^{corr})$  exactly cancels that of  $(\mathbf{w}^{near}, q^{near})$ . Consequently the sums  $\mathbf{w} = \mathbf{w}^{near} + \mathbf{w}^{corr}$  and  $q = q^{near} + q^{corr}$  form a solution to the BVP (30)–(35), hence give the periodic Green’s function. By taking  $\mathbf{f} = (1, 0)$  and  $\mathbf{f} = (0, 1)$ , and letting  $\mathbf{G}_{corr} = [\mathbf{w}_{\mathbf{y},(1,0)}^{corr}(\mathbf{x}), \mathbf{w}_{\mathbf{y},(0,1)}^{corr}(\mathbf{x})]$ , we obtain the useful decomposition:

$$\mathbf{G}_{per}(\mathbf{x}, \mathbf{y}) = \mathbf{G}_{near}(\mathbf{x}, \mathbf{y}) + \mathbf{G}_{corr}(\mathbf{x}, \mathbf{y}). \tag{56}$$

The same decomposition holds for the pressure:

$$\mathbf{G}_{per}^p(\mathbf{x}, \mathbf{y}) = \mathbf{G}_{near}^p(\mathbf{x}, \mathbf{y}) + \mathbf{G}_{corr}^p(\mathbf{x}, \mathbf{y}). \tag{57}$$

This split is a useful tool for both the analysis and the numerical method, and will be revisited in later sections.

As in the free space case, we now can define the periodic single layer potential induced by  $\boldsymbol{\rho}(\mathbf{x}) = (\rho_1(\mathbf{x}), \rho_2(\mathbf{x}))$  on a boundary  $\Gamma$  as:

$$\mathbf{u}(\mathbf{x}) = \mathcal{S}_\Gamma^{per}[\boldsymbol{\rho}](\mathbf{x}) = \int_\Gamma \mathbf{G}_{per}(\mathbf{x}, \mathbf{y})\boldsymbol{\rho}(\mathbf{y})\,d\mathbf{y}, \quad p(\mathbf{x}) = \mathcal{S}_\Gamma^{per,p}[\boldsymbol{\rho}] = \int_\Gamma \mathbf{G}_{per}^p(\mathbf{x}, \mathbf{y})\boldsymbol{\rho}(\mathbf{y})\,d\mathbf{y}. \tag{58}$$

The associated traction is given by:

$$\mathbf{T}(\mathbf{x}) = \mathcal{S}_\Gamma^{per,t} = \int_\Gamma \mathbf{G}_{per}^t(\mathbf{x}, \mathbf{y})\boldsymbol{\rho}(\mathbf{y})\,d\mathbf{y}. \tag{59}$$

Equations (56) and (57) motivate a similar decomposition for the single layer potential:

$$\mathcal{S}_\Gamma^{per}[\boldsymbol{\rho}](\mathbf{x}) = \mathcal{S}_\Gamma^{near}[\boldsymbol{\rho}](\mathbf{x}) + \mathcal{S}_\Gamma^{corr}[\boldsymbol{\rho}](\mathbf{x}) \tag{60}$$

$$\mathcal{S}_\Gamma^{per,p}[\boldsymbol{\rho}](\mathbf{x}) = \mathcal{S}_\Gamma^{near,p}[\boldsymbol{\rho}](\mathbf{x}) + \mathcal{S}_\Gamma^{corr,p}[\boldsymbol{\rho}](\mathbf{x}), \tag{61}$$

where  $\mathcal{S}_\Gamma^{near}[\boldsymbol{\rho}](\mathbf{x})$  and  $\mathcal{S}_\Gamma^{near,p}[\boldsymbol{\rho}](\mathbf{x})$  are the sums over the near copies of the unit cell of  $\mathcal{S}_\Gamma[\boldsymbol{\rho}](\mathbf{x})$  and  $\mathcal{S}_\Gamma^p[\boldsymbol{\rho}](\mathbf{x})$  respectively, while  $(\mathcal{S}_\Gamma^{corr}[\boldsymbol{\rho}](\mathbf{x}), \mathcal{S}_\Gamma^{corr,p}[\boldsymbol{\rho}](\mathbf{x}))$  is a solution to the empty box BVP (38)–(43), with the discrepancy vector  $\mathbf{g} = [\mathbf{g}_1; \mathbf{g}_2; \mathbf{g}_3; \mathbf{g}_4]$  given by:

$$\mathbf{g}_1 = -(\mathcal{S}_{\Gamma,R}^{near} - \mathcal{S}_{\Gamma,L}^{near}) \tag{62}$$

$$\mathbf{g}_2 = -(\mathcal{S}_{\Gamma,R}^{near,t} - \mathcal{S}_{\Gamma,L}^{near,t}) + \mathbf{F}/2|\mathbf{e}_2| \tag{63}$$

$$\mathbf{g}_3 = -(\mathcal{S}_{\Gamma,U}^{near} - \mathcal{S}_{\Gamma,D}^{near}) \tag{64}$$

$$\mathbf{g}_4 = -(\mathcal{S}_{\Gamma,U}^{near,t} - \mathcal{S}_{\Gamma,D}^{near,t}) + \mathbf{F}/2|\mathbf{e}_1|, \tag{65}$$

where  $\mathbf{F} = \int_{\Gamma} \boldsymbol{\rho} ds$  is the net force.

**Remark 13.** The ‘‘periodic’’ single layer potential is doubly periodic in the directions  $\mathbf{e}_1$  and  $\mathbf{e}_2$  if and only if the net force  $\mathbf{F} = \int_{\Gamma} \boldsymbol{\rho} ds = \mathbf{0}$ . In the general case where this condition is violated, the velocity field remains doubly periodic while the traction acquires a constant jump across the walls.

**Remark 14.** The difference between the periodic single layer potential and its free space counterpart is smooth in  $\mathcal{U}$ . Thus the jump relation of the single layer potential as stated in Lemma 6 holds without any changes. In fact, the properties stated in Lemma 7 also generalize directly to the periodic case. To prove this statement, we require the following lemma.

**Lemma 15.** Let  $(\mathbf{u}^{corr}, p^{corr})$  be the correction terms implied by (60) and (61). They do not contribute to the net force, net torque, or the net flux. More specifically, we have

$$\int_{\Gamma} \mathbf{T}(\mathbf{u}^{corr}, p^{corr}) ds = 0 \tag{66}$$

$$\int_{\Gamma} \left( (\mathbf{x} - \mathbf{x}^c)^\perp, \mathbf{T}(\mathbf{u}^{corr}, p^{corr}) \right) ds = 0 \tag{67}$$

$$\int_{\Gamma} \mathbf{u}^{corr} \cdot \mathbf{n} ds = 0, \tag{68}$$

where  $\Gamma = \partial\Omega$ ,  $\Omega \in \mathcal{U}$  is any domain in the unit cell.

**Proof.** Let  $D = \mathcal{U} \setminus \overline{\Omega}$ , and recall the divergence theorem for the Stokes equation:

$$\int_D (-\mu \Delta \mathbf{u}^{corr} + \nabla p^{corr}) d\mathbf{x} = - \int_{\partial D} \mathbf{T}(\mathbf{u}^{corr}, p^{corr}) ds. \tag{69}$$

Since  $(\mathbf{u}^{corr}, p^{corr})$  satisfies the Stokes equation in  $D$ , the left hand side vanishes. And the right hand side can be expanded into:

$$\int_{\partial D} \mathbf{T}(\mathbf{u}^{corr}, p^{corr}) ds = \int_{\partial \mathcal{U}} \mathbf{T}(\mathbf{u}^{corr}, p^{corr}) ds - \int_{\Gamma} \mathbf{T}(\mathbf{u}^{corr}, p^{corr}) ds \tag{70}$$

$$= - \int_{\Gamma} \mathbf{T}(\mathbf{u}^{corr}, p^{corr}) ds, \tag{71}$$

which implies (66).

The proof of (67) relies on Green’s first identity for the Stokes equation:

$$\int_{\mathcal{K}} \sum_{i=1}^2 (\mu \Delta u_i - \partial_i p) v_i = -\frac{\mu}{2} \int_{\mathcal{K}} \sum_{i,j=1}^2 (\partial_i u_j + \partial_j u_i) (\partial_i v_j + \partial_j v_i) + \int_{\partial \mathcal{K}} \sum_{i=1}^2 T_i(\mathbf{u}, p) v_i \tag{72}$$

where  $\mathcal{K}$  is an arbitrary domain. By taking  $\mathcal{K} = D$ ,  $(\mathbf{u}, p) = (\mathbf{u}^{corr}, p^{corr})$  and  $\mathbf{v} = (\mathbf{x} - \mathbf{x}^c)^\perp$ , we have:

$$\partial_i v_j + \partial_j v_i = 0, \quad i, j = 1, 2 \tag{73}$$

$$\int_D \sum_{i=1}^2 (\mu \Delta u_i - \partial_i p) v_i = 0 \tag{74}$$

$$\int_{\partial \mathcal{U}} \sum_{i=1}^2 T_i(\mathbf{u}, p) v_i = 0, \tag{75}$$

leading to  $\int_{\Gamma} \left( (\mathbf{x} - \mathbf{x}^c)^\perp, \mathbf{T}(\mathbf{u}^{corr}, p^{corr}) \right) ds = 0$ .

(68) is a direct consequence of the divergence theorem and the periodicity of  $\mathbf{u}^{corr}$ :

$$\int_{\Gamma} \mathbf{u}^{corr} \cdot \mathbf{n} ds = \int_{\partial \mathcal{U}} \mathbf{u}^{corr} \cdot \mathbf{n} ds = \int_{\mathcal{U}} \nabla \cdot \mathbf{u}^{corr} d\mathbf{x} = 0. \quad \square \tag{76}$$

### 5. Integral equation representation of the mobility BVP

The above definitions and analysis enables us to seek a solution  $(\mathbf{u}, p)$  to the quasi-static BVP in the form of a periodic single layer potential. Our ansatz is that it is represented by unknown density functions  $\boldsymbol{\rho}_i(\mathbf{x})$  on each boundary  $\Gamma_i$ . Recalling that each density  $\boldsymbol{\rho}_i(\mathbf{x})$  is a vector function  $\boldsymbol{\rho}_i(\mathbf{x}) = (\rho_{i1}(\mathbf{x}), \rho_{i2}(\mathbf{x}))$ , we stack the set of unknown scalar functions as follows,

$$\boldsymbol{\rho}(\mathbf{x}) = (\rho_{11}(\mathbf{x}), \rho_{12}(\mathbf{x}), \dots, \rho_{N_o,1}(\mathbf{x}), \rho_{N_o,2}(\mathbf{x})). \tag{77}$$

This density induces, via the periodized single-layer potential, the flow and pressure fields

$$\mathbf{u}(\mathbf{x}) = \mathcal{S}_{\Gamma}^{per}[\boldsymbol{\rho}](\mathbf{x}) := \sum_{i=1}^{N_o} \mathcal{S}_{\Gamma_i}^{per}[\boldsymbol{\rho}_i](\mathbf{x}) \tag{78}$$

$$p(\mathbf{x}) = \mathcal{S}_{\Gamma}^{per,p}[\boldsymbol{\rho}](\mathbf{x}) := \sum_{i=1}^{N_o} \mathcal{S}_{\Gamma_i}^{per,p}[\boldsymbol{\rho}_i](\mathbf{x}). \tag{79}$$

Recall that  $(\mathbf{u}, p)$  is the perturbation from plain shear flow; the physical flow is  $(\mathbf{u} + \mathbf{u}_0, p + p_0)$ . Were the above representation to result in a physical flow whose interior surface traction limit was identically zero on all of  $\Gamma := \bigcup_{i=1}^{N_o} \Gamma_i$ , then, by uniqueness of the interior traction BVP up to rigid body motions [23, Sec. 2.3.2], the representation would be a rigid flow inside each body, and would thus (by continuity of  $\mathbf{u}$ ) solve the desired quasi-static BVP. This motivates (in a precise way) the single-layer representation, with the modified boundary conditions

$$\mathbf{T}_-(\mathbf{u}, p)(\mathbf{x}) + \mathbf{T}(\mathbf{u}_0, p_0)(\mathbf{x}) = \mathbf{0} \quad \mathbf{x} \in \Gamma.$$

Notice that this differs from the common double-layer representation for velocity (Dirichlet) boundary conditions. Recalling the periodic case of the jump relation (25), applying the interior traction boundary condition gives the following Fredholm integral equation of the second kind:

$$\left(\frac{1}{2}I + \mathcal{K}\right) \boldsymbol{\rho}(\mathbf{x}) = -\mathbf{T}(\mathbf{u}_0, p_0)(\mathbf{x}), \quad \mathbf{x} \in \Gamma, \tag{80}$$

where

$$I = \begin{pmatrix} \mathbf{I}_1 & & & \\ & \mathbf{I}_2 & & \\ & & \ddots & \\ & & & \mathbf{I}_{N_o} \end{pmatrix}, \tag{81}$$

and

$$\mathcal{K} = \begin{pmatrix} \mathcal{K}_{1,1} & \mathcal{K}_{1,2} & \dots & \mathcal{K}_{1,N_o} \\ \mathcal{K}_{2,1} & \mathcal{K}_{2,2} & \dots & \mathcal{K}_{2,N_o} \\ \vdots & \vdots & \ddots & \vdots \\ \mathcal{K}_{N_o,1} & \mathcal{K}_{N_o,2} & & \mathcal{K}_{N_o,N_o} \end{pmatrix}. \tag{82}$$

Here each  $\mathcal{K}_{ij}$  is the periodic single layer traction operator from the  $j$ th boundary component to the  $i$ th boundary component, which is given by:

$$\mathcal{K}_{ij}[\boldsymbol{\rho}_j](\mathbf{x}) = \mathcal{S}_{\Gamma_j}^{per,t}[\boldsymbol{\rho}_j](\mathbf{x}) = \int_{\Gamma_j} \mathbf{G}_{per}^t(\mathbf{x}, \mathbf{y}) \boldsymbol{\rho}_j(\mathbf{y}) ds_{\mathbf{y}}, \quad \mathbf{x} \in \Gamma_i, i \neq j, \tag{83}$$

and the self-interaction operators are

$$\mathcal{K}_{ii}[\boldsymbol{\rho}_i](\mathbf{x}) = \mathcal{S}_{\Gamma_i}^{per,t}[\boldsymbol{\rho}_i](\mathbf{x}) = \oint_{\Gamma_i} \mathbf{G}_{per}^t(\mathbf{x}, \mathbf{y}) \boldsymbol{\rho}_i(\mathbf{y}) ds_{\mathbf{y}}, \quad \mathbf{x} \in \Gamma_i. \tag{84}$$

Equations (26), (27) and (28) (the periodic version) enable us to reformulate the force and torque constraints as:

$$\int_{\Gamma_i} \boldsymbol{\rho}_i(\mathbf{x}) ds_{\mathbf{x}} = \mathbf{0} \tag{85}$$

$$\int_{\Gamma_i} \left( (\mathbf{x} - \mathbf{x}_i^c)^\perp, \boldsymbol{\rho}_i(\mathbf{x}) \right) ds_{\mathbf{x}} = 0. \tag{86}$$

Following [38], we use the following rank-three perturbation operator  $\mathcal{L}_i$ , defined on  $\Gamma_i$ , associated with the above constraints on the  $i$ th body,

$$\mathcal{L}_i \boldsymbol{\rho}_i(\mathbf{x}) := \int_{\Gamma_i} \boldsymbol{\rho}_i(\mathbf{y}) ds_{\mathbf{y}} + (\mathbf{x} - \mathbf{x}_i^c)^\perp \int_{\Gamma_i} \left( (\mathbf{y} - \mathbf{x}_i^c)^\perp, \boldsymbol{\rho}_i(\mathbf{y}) \right) ds_{\mathbf{y}}, \quad \mathbf{x} \in \Gamma_i, \tag{87}$$

and also define the rank- $3N_o$  block-diagonal operator  $\mathcal{L}$  by

$$\mathcal{L} = \begin{pmatrix} \mathcal{L}_1 & & & \\ & \mathcal{L}_2 & & \\ & & \ddots & \\ & & & \mathcal{L}_{N_o} \end{pmatrix}. \tag{88}$$

It is straightforward to verify that if  $\boldsymbol{\rho}(\mathbf{x})$  satisfies equations (80), (85) and (86), then the representation  $(\mathbf{u}, p) = (S_\Gamma^{per}[\boldsymbol{\rho}], S_\Gamma^{per,p}[\boldsymbol{\rho}])$  solves the BVP (3)–(9). In particular, (85) implies that the total force  $\sum_{i=1}^{N_o} \int_{\Gamma_i} \boldsymbol{\rho}_i ds_{\mathbf{x}} = \mathbf{0}$ , so that  $\mathbf{u}$  generated by the generalized Green's function is actually periodic. Here the operator  $(\frac{1}{2}I + \mathcal{K})$  has a  $3N_o$ -dimensional null space. The purpose of the  $3N_o$  constraints is to select the particular solution with zero net forces and torques on all bodies. However this constrained BIE, when discretized, leads to a rectangular linear system that is less favorable than a square one. Thus, following [26,38], we propose instead to solve the following perturbed integral equation, which turns out to be full rank and require no additional constraints:

$$\left( \frac{1}{2}I + \mathcal{K} + \mathcal{L} \right) \boldsymbol{\rho}(\mathbf{x}) = -\mathbf{T}(\mathbf{u}_0, p_0)(\mathbf{x}), \quad \mathbf{x} \in \Gamma, \tag{89}$$

or, writing out explicitly the interactions between all pairs of bodies,

$$\begin{aligned} \frac{1}{2} \boldsymbol{\rho}_i(\mathbf{x}) + \sum_{j=1}^{N_o} \mathcal{K}_{i,j} \boldsymbol{\rho}_j(\mathbf{x}) + \int_{\Gamma_i} \boldsymbol{\rho}_i(\mathbf{y}) ds_{\mathbf{y}} + (\mathbf{x} - \mathbf{x}_i^c)^\perp \int_{\Gamma_i} \left( (\mathbf{y} - \mathbf{x}_i^c)^\perp, \boldsymbol{\rho}_i(\mathbf{y}) \right) ds_{\mathbf{y}} \\ = -\mathbf{T}(\mathbf{u}_0, p_0)(\mathbf{x}), \quad \mathbf{x} \in \Gamma_i, \quad i = 1, \dots, N_o. \end{aligned} \tag{90}$$

It is trivial to verify that equations (80), (85) and (86) imply (89). [38, Lemma 8] proved in the free space case that they are in fact equivalent. The same statement holds for the periodic case. Here we state it as a lemma and leave the proof, which is very similar to the free space case, to the reader.

**Lemma 16.** *If  $\boldsymbol{\rho}$  solves (89), then it solves (80), (85) and (86).*

The next theorem establishes the existence and uniqueness of the boundary integral equation (89), which further implies the existence of a solution to the quasi-static BVP.

**Theorem 17.** *The boundary integral equation (89) has a unique solution.*

**Proof.** We first prove that the operator  $\frac{1}{2}I + \mathcal{K} + \mathcal{L}$  is injective, following [37, Lemma 18] (this is the arXiv rather than published manuscript; also see [10, Lemma 5] for a 3D free-space version). Let  $\boldsymbol{\rho}$  solve  $(\frac{1}{2}I + \mathcal{K} + \mathcal{L})\boldsymbol{\rho} = \mathbf{0}$ . Since, for any  $\boldsymbol{\rho}$ , by the jump relations,  $(\frac{1}{2}I + \mathcal{K})\boldsymbol{\rho}$  is the interior limit of the traction  $\mathbf{T}_-(\mathbf{u}, p)$  of  $(\mathbf{u}, p)$  given by (78)–(79), then applying the periodic versions of (26) and (28) we get that  $\boldsymbol{\rho}$  satisfies the force and torque constraints (85)–(86). Thus  $\mathcal{L}\boldsymbol{\rho} = \mathbf{0}$ , and so  $(\frac{1}{2}I + \mathcal{K})\boldsymbol{\rho} = \mathbf{0}$ , which means that  $(\mathbf{u}, p)$  solves the interior traction BVP in each body with homogeneous data, thus is rigid inside each body. Thus by continuity of  $\mathbf{u}$  across  $\Gamma$ ,  $(\mathbf{u}, p)$  is a solution to the homogeneous quasi-static BVP, i.e. (3)–(9) with  $\mathbf{u}_0 \equiv \mathbf{0}$ . Thus by Lemma 4,  $\mathbf{u}$  is constant in the exterior, and by continuity, the same constant in the body interiors, thus by the traction jump relation,  $\boldsymbol{\rho} = \mathbf{T}_- - \mathbf{T}_+ \equiv \mathbf{0}$ . Having proved uniqueness, by the Fredholm alternative a solution exists for each right-hand side.  $\square$

**Theorem 18.** *There exists a solution to the quasi-static BVP (3)–(9).*

**Proof.** Let  $\rho$  be a solution to the BIE (89). Then one may check that  $\mathbf{u}(\mathbf{x}) = \mathcal{S}_\Gamma^{per}[\rho](\mathbf{x})$  and  $p(\mathbf{x}) = \mathcal{S}_\Gamma^{per,p}[\rho](\mathbf{x})$  from (78)–(79) solve the BVP.  $\square$

When combined with Lemma 4, this completely characterizes existence and uniqueness for the quasi-static BVP, we believe for the first time in the periodic setting.

### 6. Numerical solution of the BIE

In this section, we discuss the numerical solution of the BIE (90). We assume that on each boundary component  $\Gamma_i$ , we are given a set of quadrature nodes  $\{\mathbf{x}_i^{(k)}\}_{k=1}^{N_i}$  and weights  $\{w_i^{(k)}\}_{k=1}^{N_i}$  such that

$$\int_{\Gamma_i} f(\mathbf{x}) ds_{\mathbf{x}} \approx \sum_{k=1}^{N_i} f(\mathbf{x}_i^{(k)}) w_i^{(k)}$$

holds to high accuracy for smooth functions  $f$ . In our examples the boundary  $\Gamma_i$  is parametrized by a  $2\pi$ -periodic function  $\mathbf{x}_i(t)$ ,  $0 \leq t \leq 2\pi$ , so we use the periodic trapezoidal rule in  $t$ , giving  $\mathbf{x}_i^{(k)} = \mathbf{x}_i(2\pi k/N_i)$  and  $w_i^{(k)} = (2\pi/N_i) \|\mathbf{x}'_i(2\pi k/N_i)\|$ .

It is a well known fact in potential theory that the single layer traction operator  $\mathcal{K}$  is smooth, as is the operator  $\mathcal{L}$ . Thus we apply the standard Nyström discretization to the BIE, i.e. enforce (90) at the same nodes  $\{\mathbf{x}_i^{(k)} : k = 1, \dots, N_i, i = 1, \dots, N_o\}$  to get:

$$\begin{aligned} \frac{1}{2} \rho_i^k + \sum_{j=1}^{N_o} \sum_{l=1}^{N_j} \mathbf{G}_{per}^t(\mathbf{x}_k^{(i)}, \mathbf{x}_l^{(j)}) \rho_j^l w_l^{(j)} + \sum_{m=1}^{N_i} \rho_i^m w_m^{(i)} + (\mathbf{x}_k^{(i)} - \mathbf{x}_i^c)^\perp \cdot \sum_{m=1}^{N_i} \left( (\mathbf{x}_m^{(i)} - \mathbf{x}_i^c)^\perp, \rho_i^m \right) w_m^{(i)} \\ = \mathbf{T}(\mathbf{u}_0, p_0)(\mathbf{x}_k^{(i)}), \quad k = 1, \dots, N_i, i = 1, \dots, N_o, \end{aligned} \quad (91)$$

where  $\rho_i^k = (\rho_{i1}^k, \rho_{i2}^k) := \rho_i(\mathbf{x}_i^{(k)}) = (\rho_{i1}(\mathbf{x}_i^{(k)}), \rho_{i2}(\mathbf{x}_i^{(k)}))$ . This is a square linear system of size  $2N_i N_o$ .

To complete the numerical method, several problems remain to be addressed. We discuss them in details in the following subsections.

#### 6.1. Numerical methods for the empty box BVP

As mentioned in previous sections, numerical solution of the empty box BVP (38)–(43) is a necessary correction term in the evaluation of the periodic Green’s function. There exist an abundance of methods for this problem. We find it simple, efficient, and accurate to solve it by the method of fundamental solutions (MFS).

Defining the tensor function  $\phi_j(\mathbf{x}) := \mathbf{G}(\mathbf{x}, \mathbf{y}_j)$  and vector function  $\phi_j^p(\mathbf{x}) := \mathbf{G}^p(\mathbf{x}, \mathbf{y}_j)$ , where  $\mathbf{G}(\mathbf{x}, \mathbf{y})$  and  $\mathbf{G}^p(\mathbf{x}, \mathbf{y})$  are the free space Green’s functions for velocity and pressure, and  $\{\mathbf{y}_j\}_{j=1}^M$  are a collection of points lying on the walls of the expanded unit cell  $\tilde{\mathcal{U}}$ , we approximate the solution in  $\mathcal{U}$  by a linear combination of such functions:

$$\mathbf{v}(\mathbf{x}) \approx \sum_{j=1}^M \phi_j(\mathbf{x}) \xi_j, \quad \mathbf{x} \in \mathcal{U} \quad (92)$$

$$q(\mathbf{x}) \approx \sum_{j=1}^M \phi_j^p(\mathbf{x}) \cdot \xi_j, \quad \mathbf{x} \in \mathcal{U} \quad (93)$$

Here  $\{\xi_j\}_{j=1}^M$  are unknown vectors in  $\mathbb{R}^2$ . Since each basis function is a solution to the Stokes equation (38)–(39), it remains only to enforce the boundary conditions (40)–(43).

The  $2M$  unknowns in the coefficient vector  $\xi := \{\xi_j\}_{j=1}^M$  are determined by matching conditions as follows. We let  $\{\mathbf{x}_{iL}\}_{j=1}^m \subset L$  and  $\{\mathbf{x}_{iD}\}_{j=1}^m \subset D$  be two sets of  $m$  collocation points (Gauss–Legendre nodes, for example) on the left and bottom walls respectively. Then, enforcing just (40) on the left wall gives

$$\sum_{j=1}^M [\phi_j(\mathbf{x}_{iL} + \mathbf{e}_1) - \phi_j(\mathbf{x}_{iL})] \xi_j = \mathbf{g}_1(\mathbf{x}_{iL}), \quad i = 1, \dots, m, \quad (94)$$

which can be summarized by  $Q_1 \xi = d_1$ , where  $Q_1 = [Q_1^{11}, Q_1^{12}; Q_1^{21}, Q_1^{22}]$ , with each block having entries  $(Q_1^{kl})_{ij} = \phi_j^{kl}(\mathbf{x}_{iL} + \mathbf{e}_1) - \phi_j^{kl}(\mathbf{x}_{iL})$ , and  $d_1 := \{\mathbf{g}_1(\mathbf{x}_{iL})\}_{i=1}^m$ . We order the vectors with all the 1-components followed by all the 2-components.

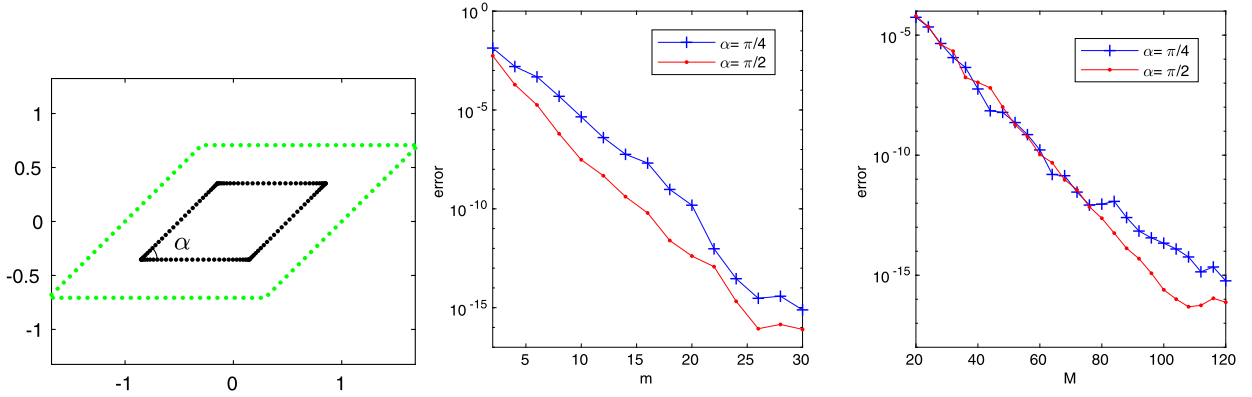


**Fig. 3.** Convergence study of the empty box BVP. (Left) shows the collocation points on the walls and the proxy points (on the expanded unit cell). (Middle) shows the relative  $L^\infty$  error vs the number of collocation points. (Right) shows the relative  $L^\infty$  error vs the number of proxy points.

Repeating this bookkeeping routine for the other three periodicity conditions (41)–(43), we get the linear system

$$Q \xi = d, \tag{95}$$

where  $Q = [Q_1; Q_2; Q_3; Q_4]$  and  $d = [d_1; d_2; d_3; d_4]$ , and each block corresponds to one of the conditions. This small dense linear system (which is generally rectangular and ill-conditioned) is then solved in the least square sense. A convergence test is given in Fig. 3.

**Remark 19.** The method we presented here is similar to that in [2], except that by using the expanded unit cell as the “proxy surface” we improve the robustness of the solution for skewed unit cells with a wide range of aspect ratios.

The system matrix  $Q$  inherits the consistency conditions (48) and (49), which in terms of linear algebra, can be stated as

$$W^T Q \approx \mathbf{0}_{3 \times 2M}, \tag{96}$$

where

$$W^T = \begin{bmatrix} 0 & 0 & \mathbf{w}_L^T & 0 & 0 & 0 & \mathbf{w}_D^T & 0 \\ 0 & 0 & 0 & \mathbf{w}_L^T & 0 & 0 & 0 & \mathbf{w}_D^T \\ \mathbf{w}_L^T \mathbf{e}_1^T & \mathbf{w}_L^T \mathbf{e}_2^T & 0 & 0 & \mathbf{w}_D^T \mathbf{e}_1^T & \mathbf{w}_D^T \mathbf{e}_1^T & 0 & 0 \end{bmatrix} \in \mathbb{R}^{3 \times 8m}. \tag{97}$$

**Example 1.** As a verification of the method, we solve the EBVP with the discrepancy vector  $\mathbf{g}$  generated by a known solution, in unit cells with different aspect ratios. More specifically, we fix  $\mu = 0.7$ ,  $\mathbf{y}_0 = 1.5(\cos 0.1, \sin 0.1)$ , and  $\mathbf{f}_0 = (0.3, -0.6)$ , and let  $\mathbf{v}(\mathbf{x}) = \mathbf{G}(\mathbf{x}, \mathbf{y}_0)\mathbf{f}_0$ , and  $q(\mathbf{x}) = \mathbf{G}^p(\mathbf{x}, \mathbf{y}_0) \cdot \mathbf{f}_0$ . In the first example, we choose the unit cell to be the unit square centered at the origin with  $\mathbf{e}_1 = (1, 0)$  and  $\mathbf{e}_2 = (0, 1)$ . In the second example, we change  $\mathbf{e}_2$  to be  $(\cos \frac{\pi}{4}, \sin \frac{\pi}{4})$ , while keeping the center and  $\mathbf{e}_1$  unchanged.

In both cases,  $\mathbf{g}$  is generated by evaluating  $\mathbf{v}(\mathbf{x})$  and  $\mathbf{T}(\mathbf{v}, q)(\mathbf{x})$  on the walls, and the resulting EBVP is solved by the MFS. The solution is computed on a  $100 \times 100$  grid in the unit cell and the error is obtained by comparing the computed solution to the exact one. The error at the first grid point is subtracted to account for the fact that the solution is unique only up to a constant.

The results are given in Fig. 3, which shows the convergence in the number  $m$  of the collocation points on each wall, and in the number  $M$  of proxy points. In both cases, we observe an exponential convergence in both  $m$  and  $M$ . The numbers required to achieve high accuracy are small, and relatively insensitive to the aspect ratio.

### 6.2. Evaluation of the periodic Green's function

To solve (91) iteratively, the periodized Green's function must be applied to arbitrary trial vectors. This amounts to evaluation of sums of the following forms at the entire set of surface targets  $i = 1, \dots, N$ , for some large  $N$ .

$$S_{per}(\mathbf{x}_i) = \sum_{j=1}^N \mathbf{G}_{per}(\mathbf{x}_i, \mathbf{y}_j)\mathbf{f}_j \tag{98}$$

$$S_{per}^p(\mathbf{x}_i) = \sum_{j=1}^N \mathbf{G}_{per}^p(\mathbf{x}_i, \mathbf{y}_j) \cdot \mathbf{f}_j \tag{99}$$

$$S_{per}^t(\mathbf{x}_i) = \sum_{j=1}^N \mathbf{G}_{per}^t(\mathbf{x}_i, \mathbf{y}_j) \mathbf{f}_j. \tag{100}$$

Here  $\mathbf{G}_{per}(\mathbf{x}, \mathbf{y})$  is the generalized periodic Green’s function defined in section 4.2, and  $\mathbf{G}_{per}^p(\mathbf{x}, \mathbf{y})$  and  $\mathbf{G}_{per}^t(\mathbf{x}, \mathbf{y})$  are the associated pressure and traction kernels.  $\{\mathbf{y}_j\}_{j=1}^N$  are a given set of point sources lying in the unit cell  $\mathcal{U}$ , with given strength  $\{\mathbf{f}_j\}_{j=1}^N$ , and  $\{\mathbf{x}_i\}_{i=1}^N$  are a given set of target points, also in the unit cell  $\mathcal{U}$ . We now summarize the practical use of the decompositions (56) and (57). There are four main steps:

1. Compute the “near part” of the sums at all targets,

$$S_{near}(\mathbf{x}_i) := \sum_{j=1}^N \mathbf{G}_{near}(\mathbf{x}_i, \mathbf{y}_j) \mathbf{f}_j$$

$$S_{near}^p(\mathbf{x}_i) := \sum_{j=1}^N \mathbf{G}_{near}^p(\mathbf{x}_i, \mathbf{y}_j) \mathbf{f}_j$$

$$S_{near}^t(\mathbf{x}_i) := \sum_{j=1}^N \mathbf{G}_{near}^t(\mathbf{x}_i, \mathbf{y}_j) \mathbf{f}_j.$$

This is most efficiently done using a fast algorithm such as a Stokes FMM.

2. Evaluate the discrepancy of the “near part” sums  $S_{near}(\mathbf{x})$  and  $S_{near}^t(\mathbf{x})$  at the walls, namely:  $\mathbf{g} = [\mathbf{g}_1; \mathbf{g}_2; \mathbf{g}_3; \mathbf{g}_4]$ , where

$$\mathbf{g}_1 = S_{near,R} - S_{near,L}$$

$$\mathbf{g}_2 = S_{near,R}^t - S_{near,L}^t$$

$$\mathbf{g}_3 = S_{near,U} - S_{near,D}$$

$$\mathbf{g}_4 = S_{near,U}^t - S_{near,D}^t.$$

Notice that cancellation may be exploited here, so that all evaluations are distant even when sources approach or lie on the walls.

3. Use the MFS to solve the empty box BVP with the modified discrepancy  $\tilde{\mathbf{g}} = \mathbf{g}_0 - \mathbf{g}$ , where  $\mathbf{g}_0 = [\mathbf{0}; \mathbf{F}/2|\mathbf{e}_2|; \mathbf{0}; \mathbf{F}/2|\mathbf{e}_1|]$ , for total force  $\mathbf{F} = \sum_{j=1}^N \mathbf{f}_j$ , to get the periodizing coefficients  $\{\xi_j\}_{j=1}^M$ .
4. Recover the periodic sums by evaluating the correction pair  $(\mathbf{v}, q)$  at the targets via sums (92)–(93), then adding this to the near results:

$$S(\mathbf{x}_i) = S_{near}(\mathbf{x}_i) + \mathbf{v}(\mathbf{x}_i) \tag{101}$$

$$S^p(\mathbf{x}_i) = S_{near}^p(\mathbf{x}_i) + q(\mathbf{x}_i) \tag{102}$$

$$S^t(\mathbf{x}_i) = S_{near}^t(\mathbf{x}_i) + \mathbf{T}(\mathbf{v}, q)(\mathbf{x}_i). \tag{103}$$

**Remark 20.** It is a direct consequence of Theorem 12 that the discrepancy  $\tilde{\mathbf{g}}$  obtained from the above procedure automatically satisfies the consistency conditions for the empty box BVP. In the language of linear algebra, letting  $\mathbf{d} = \{\mathbf{g}(\mathbf{y}_j)\}_{j=1}^M$  and  $\tilde{\mathbf{d}} = \{\tilde{\mathbf{g}}(\mathbf{y}_j)\}_{j=1}^M$  be the discretization of  $\mathbf{g}$  and  $\tilde{\mathbf{g}}$  respectively, we can write  $\tilde{\mathbf{d}} = P\mathbf{d}$ , where  $P$  is the projection from  $\mathbf{d}$  to  $\tilde{\mathbf{d}}$ . The statement is that  $W^T \tilde{\mathbf{d}} \approx \mathbf{0}$  holds true up to the discretization error, i.e. the vector  $\tilde{\mathbf{d}}$  always lies in the range of  $Q$ , even though  $\mathbf{d}$  in general does not.

**Remark 21 (Complexity).** Since the correction pair  $(\mathbf{v}, q)$  is smooth inside the unit cell  $\mathcal{U}$ , only  $M = O(1)$  basis functions are needed, independent of  $N$ . As a result, the linear system solves costs  $O(1)$ , while direct evaluation of the discrepancy and evaluation of the correction at the targets both cost  $O(N)$ . The FMM evaluates the “near part” in  $O(N)$  time, so that the total cost remains  $O(N)$ . In practice the total time is dominated by the near-sum FMM from  $4N$  sources to  $N$  targets.

**Remark 22 (Pressure correction for GMRES stability).** Armed with the machinery described in previous sections, we can now apply iterative methods like GMRES to solve the linear system (91), with one caveat: due to the fact that the generalized

Green’s function for the traction  $\mathbf{G}_{per}^t(\mathbf{x}, \mathbf{y})$  is determined only up to a constant  $c\mathbf{n}_x$ , a direct implementation of this algorithm results in a stagnation of GMRES. This is not an issue with ill-conditioning—recall that the underlying BIE (90) is 2nd-kind with no nullspace—rather that the *application of the system matrix* itself has a one-dimensional subspace (an overall pressure constant) which is undefined.

Fortunately this problem can be fixed easily. We introduce  $\mathbf{T}_\alpha(\mathbf{x}) = \mathbf{T}(\mathbf{x}) + \alpha\mathbf{n}_x$ , where  $\mathbf{T}(\mathbf{x}) = \mathcal{K}[\boldsymbol{\rho}]$  is the traction of the periodic single layer potential with density  $\boldsymbol{\rho}$ . Letting  $\mathbf{x}_1 \in \Gamma$  be a fixed point on some boundary, we pick  $\alpha$  so that  $\mathbf{T}_\alpha(\mathbf{x}_1) \cdot \mathbf{n}_{x_1} = 0$ , i.e.  $\alpha = -\mathbf{T}(\mathbf{x}_1) \cdot \mathbf{n}_{x_1}$ . We then replace  $\mathbf{T}(\mathbf{x}) = \mathcal{K}[\boldsymbol{\rho}]$  in the equation (89) by the modified  $\mathbf{T}_\alpha(\mathbf{x})$ . The rest of the algorithm remains unchanged. This simple correction means that GMRES “sees” a stable system matrix, preventing stagnation.

### 6.3. Special quadrature for evaluation close to the boundary

When simulating dense suspension of particles in viscous flows, we are often faced with the situations where particles approach very close to each other. In order to use integral equation methods, we need quadrature rules for the accurate evaluation of integrals in the form of (78), (79), and the corresponding traction, where the target  $\mathbf{x}$  can be arbitrarily close to the boundary  $\Gamma$ .

It is well known that a fixed smooth rule leads to the error of  $O(1)$  as  $\mathbf{x}$  approaches  $\Gamma$ . Fortunately special quadrature rules have been developed for the evaluation of layer potentials with close to surface targets. Here we recommend the exterior single-layer rule in [4], which builds upon the “globally compensated” rule of Helsing–Ojala [22]. Both exploit barycentric-type quadratures for Cauchy integrals and their derivatives.

The Stokes single layer potential evaluator is obtained by expressing the single layer potential in terms of Laplace layer potentials.

$$S[\boldsymbol{\rho}](\mathbf{x}) = \frac{1}{2}S_L[\boldsymbol{\rho}] + \frac{1}{2}\nabla S_L[\tilde{\boldsymbol{\rho}}] - \frac{1}{2}x_1\nabla S_L[\rho_1] - \frac{1}{2}x_2\nabla S_L[\rho_2], \tag{104}$$

where  $\boldsymbol{\rho} = (\rho_1, \rho_2)$ ,  $\tilde{\boldsymbol{\rho}}(\mathbf{x}) = \mathbf{x} \cdot \boldsymbol{\rho}(\mathbf{x})$ .

In our formulation, we also need to evaluate the traction of the Stokes single layer potential, for which we introduce the following decomposition to complete the story.

$$\begin{aligned} S^t[\boldsymbol{\rho}](\mathbf{x}) &= x_1\mathcal{H}_x(S_L(\rho_1)) \cdot \mathbf{n}_x + x_2\mathcal{H}_x(S_L(\rho_2)) \cdot \mathbf{n}_x \\ &\quad - \mathcal{H}_x(S_L(\tilde{\boldsymbol{\rho}})) \cdot \mathbf{n}_x - (\partial_{x_1}S[\rho_1] + \partial_{x_2}S[\rho_2]) \cdot \mathbf{n}_x, \end{aligned} \tag{105}$$

where  $\boldsymbol{\rho} = (\rho_1, \rho_2)$ ,  $\tilde{\boldsymbol{\rho}}(\mathbf{x}) = \mathbf{x} \cdot \boldsymbol{\rho}(\mathbf{x})$ , and  $\mathcal{H}_x$  is the Hessian matrix with respect to  $\mathbf{x}$ .

**Remark 23.** To further reduce the computational cost, we use the special quadrature rule in the following fashion. We divide the solver into two phases: a precomputation phase where a sparse matrix is formed, corresponding to the correction of the quadrature for points that are within  $10h$  distance from a boundary, followed by a solution phase, where GMRES is called to solve the linear system, where in each interaction an FMM is called and the sparse matrix is applied.

### 6.4. Efficient evaluation of the effective viscosity

It is important in applications to extract the effective (homogenized) viscosity, given by (14) in the case that no particle intersects  $D$ . Since physically this formula integrates the horizontal force transmitted per unit cell, and every object  $\Omega_k$  or region of fluid is in static equilibrium (Reynolds number is zero), in fact *any* curve  $\mathcal{C}$  may be used which connects a point on  $L$  to its corresponding periodic image on  $R$  yet does not touch any objects. That is,  $\int_D$  in (14) may be replaced by  $\int_{\mathcal{C}}$ ; the proof is via Gauss’ Law (26). Thus there is invariance to “deformation” of the integration contour, as in complex analysis.

Since in a large scale simulation with many particles it is common for at least one particle to be intersecting  $B$ , integration on  $D$  cannot be used. However, in this case of many particles, finding a  $\mathcal{C}$  as above, and choosing a numerical quadrature scheme sufficiently resolved to handle the rapid traction changes as  $\mathcal{C}$  passes between nearly touching objects, would be cumbersome. Thus, in the spirit of [2, Sec. 2.6], we propose a much more efficient and (we believe) elegant contour deformation method that exploits the split of the periodic BIE representation into near sum and correction parts. This method only involves *distant* interactions, thus allows  $O(1)$  quadrature nodes independent of the complexity of the geometry.

We now present a method to evaluate the force integral  $\int_{\mathcal{C}} \mathbf{T}(\mathbf{u}, p)ds_{\mathbf{x}}$ , where  $\mathcal{C}$  is a deformation of  $D$ , needed for (14). Without loss of generality, we assume that the unit cell  $\mathcal{U}$  is centered at the origin. We consider  $K = 1$  (a single object in the unit cell); the generalization to  $K > 1$  is straightforward. If this object  $\Omega$  intersects the wall  $D$ , we assume that  $\mathcal{C}$  has been deformed to pass *below*  $\Omega$ , and that its endpoints are the same as those of  $D$ . We split the boundary of  $\Omega$  as  $\Gamma = \cup_{i=1}^4 \Gamma_i$ , where  $\Gamma_i$  is the part of  $\Gamma$  that lies in the  $i$ th “quadrant” (in the sense of the skew unit cell). See Fig. 4. Define the (possibly disconnected) curve  $\tilde{\Gamma} = \cup_{i=1}^4 \tilde{\Gamma}_i$ , where  $\tilde{\Gamma}_1 = \Gamma_1 - \mathbf{e}_1 - \mathbf{e}_2$ ,  $\tilde{\Gamma}_2 = \Gamma_1 - \mathbf{e}_2$ ,  $\tilde{\Gamma}_3 = \Gamma_3$ , and  $\tilde{\Gamma}_4 = \Gamma_1 - \mathbf{e}_1$ .

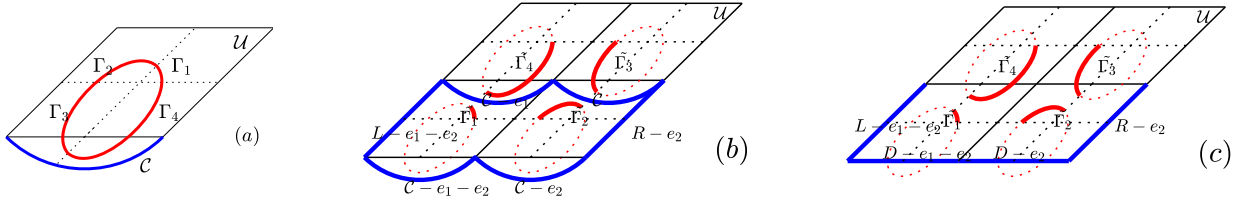


**Fig. 4.** Illustration of the deformation of contour technique for the evaluation of effective viscosity. (a) shows one unit cell  $\mathcal{U}$  with one object that intersects the bottom wall. The integration on the bottom wall can be replaced by that on the curve  $\mathcal{C}$ . (b) shows four unit cells ( $\mathcal{U}$  is in the upper-right), with the shifted pieces of the boundary (solid red) and the shifted copies of  $\mathcal{C}$  (blue). Gauss' Law is applied on the closed contour in blue, which encloses  $\tilde{\Gamma}_1$  and  $\tilde{\Gamma}_2$ . (c) shows the same four unit cells as (b) but with only the used contributions. Cancelling the terms involving shifted copies of  $\mathcal{C}$  leaves sources on the shifted pieces of the boundary and (well-separated) targets on the shifted walls (solid blue) only. (For interpretation of the colors in the figure(s), the reader is referred to the web version of this article.)

**Proposition 24.** Let  $\mathbf{T} = S_{\Gamma}^{per,t}[\boldsymbol{\rho}] = S_{\Gamma}^{near,t}[\boldsymbol{\rho}] + \mathbf{T}(\mathbf{v}, q)$  be the traction on  $\mathcal{C}$  of a periodic single layer potential that is decomposed into a near direct image sum plus a correction part given by velocity field  $\mathbf{v}$  and pressure  $q$ , as in (103). Define  $\tilde{\boldsymbol{\rho}}$  on  $\tilde{\Gamma}$  in the natural way so that  $\tilde{\boldsymbol{\rho}}|_{\tilde{\Gamma}_i} = \boldsymbol{\rho}|_{\Gamma_i}$ . Then,

$$\int_{\mathcal{C}} \mathbf{T} ds_{\mathbf{x}} = \int_{R-\mathbf{e}_2} S_{\tilde{\Gamma}}^t[\tilde{\boldsymbol{\rho}}] ds_{\mathbf{x}} - \int_{L-\mathbf{e}_1-\mathbf{e}_2} S_{\tilde{\Gamma}}^t[\tilde{\boldsymbol{\rho}}] ds_{\mathbf{x}} + 2 \int_{D-\mathbf{e}_1-\mathbf{e}_2} S_{\tilde{\Gamma}}^t[\tilde{\boldsymbol{\rho}}] ds_{\mathbf{x}} + 2 \int_{D-\mathbf{e}_2} S_{\tilde{\Gamma}}^t[\tilde{\boldsymbol{\rho}}] ds_{\mathbf{x}} - \int_{\Gamma_1 \cup \Gamma_2} \boldsymbol{\rho} ds_{\mathbf{x}} + \int_D \mathbf{T}(\mathbf{v}, q) . \tag{106}$$

**Proof.** Since the free space kernel  $\mathbf{G}^t(\mathbf{x}, \mathbf{y}) = \mathbf{G}^t(\mathbf{x} - \mathbf{y})$  is translation invariant, it is straightforward to verify that

$$S_{\Gamma}^{near,t}[\boldsymbol{\rho}](\mathbf{x}) = S_{\tilde{\Gamma}}^t[\tilde{\boldsymbol{\rho}}](\mathbf{x}) + S_{\tilde{\Gamma}}^t[\tilde{\boldsymbol{\rho}}](\mathbf{x} - \mathbf{e}_1) + S_{\tilde{\Gamma}}^t[\tilde{\boldsymbol{\rho}}](\mathbf{x} - \mathbf{e}_2) + S_{\tilde{\Gamma}}^t[\tilde{\boldsymbol{\rho}}](\mathbf{x} - \mathbf{e}_1 - \mathbf{e}_2) , \tag{107}$$

simply by fixing the sources to be  $\tilde{\Gamma}$  and shifting the targets accordingly. Integrating both sides on  $\mathcal{C}$  leads to

$$\int_{\mathcal{C}} S_{\Gamma}^{near,t}[\boldsymbol{\rho}] ds_{\mathbf{x}} = \int_D S_{\tilde{\Gamma}}^t[\tilde{\boldsymbol{\rho}}] ds_{\mathbf{x}} + \int_{\mathcal{C}-\mathbf{e}_1} S_{\tilde{\Gamma}}^t[\tilde{\boldsymbol{\rho}}] ds_{\mathbf{x}} + \int_{\mathcal{C}-\mathbf{e}_2} S_{\tilde{\Gamma}}^t[\tilde{\boldsymbol{\rho}}] ds_{\mathbf{x}} + \int_{\mathcal{C}-\mathbf{e}_1-\mathbf{e}_2} S_{\tilde{\Gamma}}^t[\tilde{\boldsymbol{\rho}}] ds_{\mathbf{x}} . \tag{108}$$

However, (26) implies

$$\int_{\mathcal{B}} S_{\tilde{\Gamma}}^t[\tilde{\boldsymbol{\rho}}] ds_{\mathbf{x}} = \int_{\tilde{\Gamma}_1 \cup \tilde{\Gamma}_2} \tilde{\boldsymbol{\rho}} ds_{\mathbf{x}} = \int_{\Gamma_1 \cup \Gamma_2} \boldsymbol{\rho} ds_{\mathbf{x}} , \tag{109}$$

where  $\mathcal{B}$  is the closed loop given by the six curves  $L - \mathbf{e}_1 - \mathbf{e}_2$ ,  $\mathcal{C} - \mathbf{e}_1 - \mathbf{e}_2$ ,  $\mathcal{C} - \mathbf{e}_2$ ,  $R - \mathbf{e}_2$ ,  $\mathcal{C}$ , and  $\mathcal{C} - \mathbf{e}_1$ , oriented in the counterclockwise sense. Note that  $\mathcal{B}$  is the boundary of the two (deformed) unit cells  $\mathcal{U} - \mathbf{e}_1 - \mathbf{e}_2 \cup \mathcal{U} - \mathbf{e}_2$ , and encloses the sources  $\tilde{\Gamma}_1$  and  $\tilde{\Gamma}_2$ , giving (109). See Fig. 4. We now add (108) and (109), and observe cancellations of the wall terms  $\mathcal{C}$  and  $\mathcal{C} - \mathbf{e}_1$ , leaving (106) except with  $\mathcal{C}$  in place of  $D$  on the right-hand side. Finally, since they are around half a unit cell from any sources,  $\mathcal{C}$  and  $\mathcal{C} - \mathbf{e}_1$  may be deformed back to  $D$  and  $D - \mathbf{e}_1$  respectively without any effect.  $\mathcal{C}$  may similarly be replaced by  $D$  in the final correction term of (106) because  $(\mathbf{v}, q)$  is a Stokes pair throughout a neighborhood of  $\mathcal{U}$ .  $\square$

**Remark 25.** The formula (106) involves integration in the far field of source curves only (all distances are at least half a unit cell), and the term involving  $\mathbf{v}$  is also smooth. As a consequence, a smooth quadrature rule with  $O(1)$  nodes is enough to compute it accurately. In addition, a little bookkeeping shows that the values of  $S_{\tilde{\Gamma}}^t[\tilde{\boldsymbol{\rho}}]$  on the four shifted walls  $R - \mathbf{e}_2$ ,  $R - \mathbf{e}_1 - \mathbf{e}_2$ ,  $L - \mathbf{e}_1 - \mathbf{e}_2$ , and  $D - \mathbf{e}_1 - \mathbf{e}_2$  also appear when forming the discrepancy vector. Consequently no extra cost is needed in evaluating  $S_{\tilde{\Gamma}}^t[\tilde{\boldsymbol{\sigma}}]$  at the quadrature nodes. They are readily available as a byproduct of the periodization by the MFS.

### 7. Time evolution and time stepping

So far we have presented the solution of the quasi-static problem for a given unit cell and particle geometry. Recall that the quasi-static solver takes as input the viscosity  $\mu$ , the shear rate  $\gamma$ , the current lattice vectors  $\mathbf{e}_1$  and  $\mathbf{e}_2$ , and the current boundaries of the rigid particles  $\{\Gamma_j\}_{j=1}^{N_0}$ , and returns the linear velocities of the particles  $\{\mathbf{v}_j\}_{j=1}^{N_0}$ , their angular velocities  $\{\omega_j\}_{j=1}^{N_0}$ , and the velocity field  $\mathbf{u}(\mathbf{x})$  and pressure  $p(\mathbf{x})$  for  $\mathbf{x} \in \mathcal{U} \setminus \overline{\Omega_{\Lambda}}$ . However, the effects of the evolving particle positions and angles, and the resulting changes in viscosity, are more of interest.

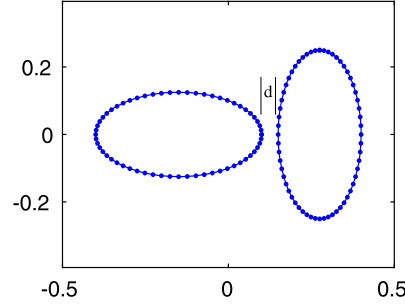


Fig. 5. Geometry for Example 1: two ellipses with aspect ratio 2 that are a small distance  $d$  apart.

We assume that the background flow is shearing in the  $y$ -direction at a constant rate  $\gamma$ , so have  $\mathbf{e}_1(t) = (1, 0)$  and  $\mathbf{e}_2(t) = (\gamma t - \text{round}(\gamma t), 1)$ , where  $\text{round}(x)$  is defined as the integer nearest to  $x \in \mathbb{R}$ . Here the rounding operation causes  $\mathbf{e}_2(t)$  to jump backwards, once per shear time, in a way that remains consistent with the periodicity of the lattice of particles. This ensures a lattice whose skewness remains bounded. (More general prescribed time-dependent shear of a general unit cell is of course possible, as long as the skewness is kept small in a similar fashion.) Let  $\{\mathbf{x}_j^c(t)\}_{j=1}^{N_o}$  and  $\{\theta_j(t)\}_{j=1}^{N_o}$  be the centers and angles of the particles, whose initial configuration was  $\{\Gamma_j(0)\}_{j=1}^{N_o}$ . Since particle shapes remain unchanged in time, there exists a fixed function  $\mathbf{X}_b$  that maps the centers and angles to the boundaries:  $\Gamma_j = \mathbf{X}_b(\mathbf{x}_j^c, \theta_j)$ . We further assume that the function  $\mathbf{X}_b$  is given explicitly and at  $t = 0$  the initial values of the centers and angles are given by  $\mathbf{x}_{j,0}^c$  and  $\theta_{j,0}^c$ .

We stack the centers and angles into one vector  $\mathbf{s} = (\mathbf{x}_1^c, \dots, \mathbf{x}_{N_o}^c, \theta_1, \dots, \theta_{N_o})$ , and observe that  $\mathbf{v}_j = \frac{d\mathbf{x}_j^c}{dt}$ , and  $\omega_j = \frac{d\theta_j}{dt}$ . Using these notations, we can reinterpret the quasi-static solver as a function  $F$  that maps  $(t, \mathbf{s})$  to the velocity  $\frac{d\mathbf{s}}{dt}$ , leading to the following standard first-order ODE system that governs the evolution:

$$\begin{cases} \frac{d\mathbf{s}}{dt} = F(t, \mathbf{s}) \\ \mathbf{s}(0) = \mathbf{s}_0. \end{cases} \quad (110)$$

In our case of constant shear rate, this ODE is autonomous.

Many numerical methods for ODEs can be applied, the simplest one being Forward Euler, which leads to  $s^{(n+1)} = s^{(n)} + \Delta t F(t_n, s^{(n)})$ , where  $s^{(n)} := s(t_n)$ . Higher order and/or adaptive methods can also be applied [31] but with one caveat: when objects become too close to each other (here, less than  $\mathcal{O}(h^2)$ ), accuracy is lost in the quasi-static solve, limiting the accuracy of the time evolution. In practice it is common to add non-hydrodynamic short-range repulsion forces, or non-overlapping constraints [47], in such simulations; however, that is beyond the scope of this paper. Instead, since much of our focus is on the fast quasi-static solver, we study only Forward Euler with various fixed time-steps.

## 8. Numerical examples

**Example 1.** As a first example, we carry out a convergence study for the quasi-static problem. We define the boundaries to be two ellipses  $\Gamma_1 : \{(x_1 + 0.25 \cos \theta, 0.125 \sin \theta), \theta \in [0, 2\pi]\}$ , and  $\Gamma_2 : \{(x_2 + 0.125 \cos \theta, 0.25 \sin \theta), \theta \in [0, 2\pi]\}$ .  $x_1$  and  $x_2$  are chosen so that  $\Gamma_1$  and  $\Gamma_2$  are distance  $d$  apart, i.e.  $|x_1 - x_2| = d + 0.375$ . It is well known that as  $d$  shrinks, the traction becomes more and more sharply peaked, requiring more discretization points on the boundary. In fact it is pointed out in [39,45] that the width of the ‘‘bump’’ scales as  $O(\sqrt{d/\kappa})$ , where  $\kappa = \kappa_1 + \kappa_2$  is the sum of the curvatures of the boundaries at the close to touching point.

In this example, we have carried out experiments for  $d = 10^{-1}, 10^{-3}, 10^{-5}$ , each for different numbers of discretization points on the boundaries. Results are shown in Fig. 6 where we measure the resolution by the residuals from recovering the rigid body motion as well as the errors in the linear and angular velocities. In all the experiments, we set the tolerance of the FMM to be  $10^{-12}$  and the tolerance for the GMRES to be  $10^{-10}$ . The reference solution is computed with  $10^4$  points on the boundary.

A spectral convergence is observed in each case. The onset of the convergence shows a  $O(1/\sqrt{d})$  scaling with respect to the distance, consistent with the asymptotic analysis. In the  $d = 10^{-1}$  case, it requires around 60 points to achieve an error of  $10^{-12}$ , while in the  $d = 10^{-5}$  case, it requires around 6000 points to get an error of  $10^{-8}$ , demonstrating the robustness of our method for close-to-touching boundaries.

**Example 2.** In this example, we demonstrate the efficiency of our solver for the quasi-static BVP with complex geometry. We create a large number  $K$  of random geometries where each boundary takes the form  $r(\theta) = s(1 + a \cos \omega \theta + \phi)$ , with  $\phi$  random, uniformly in  $[0, 0.5]$ ,  $\omega$  randomly chosen from  $\{2, 3, 4, 5\}$ , and  $s$  varying over a size ratio of 4. They are then scaled

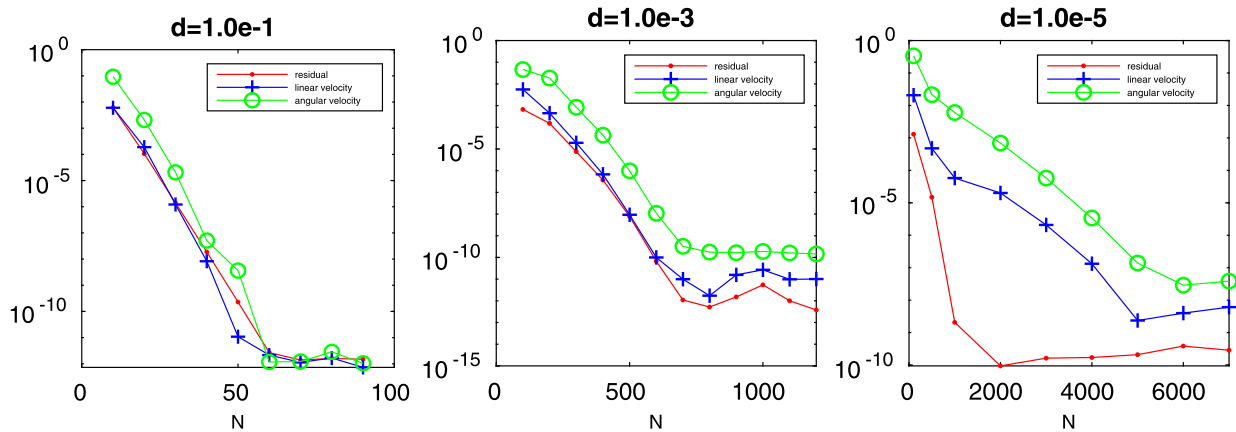


**Fig. 6.** Convergence study for the quasi-static BVP, where the boundaries are two ellipses placed at a certain distance apart (Example 1). In all three plots,  $N$  is the number of points on each ellipse. A spectral convergence in  $N$  is observed in each case, while the onset  $N$  of the convergence is seen to scale as  $O(1/\sqrt{d})$ .

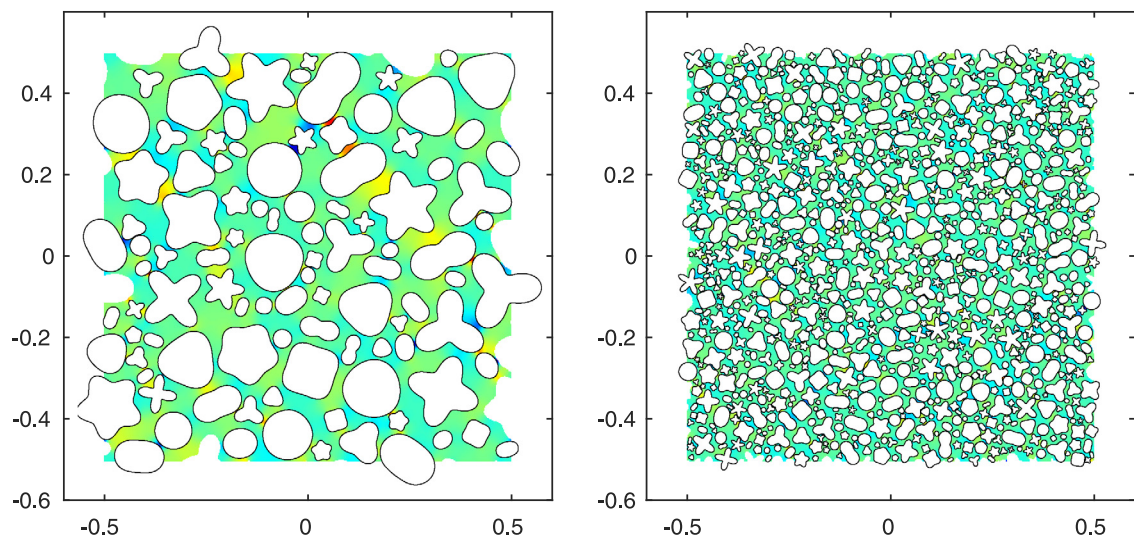


**Fig. 7.** Pressure field of the quasi-static BVP with complex boundaries (Example 2). In the left plot, the boundary consists of 100 closed curves and in the right plot, there are 1000.

and shifted to fill out the unit square, where overlapping ones are discarded. The geometries with  $K = 100$  and  $K = 1000$  are shown in Fig. 7.

The quasi-static BVP with viscosity  $\mu = 0.7$  and shear rate  $\gamma = 1$  is then solved for  $K = 100, 200, \dots, 1000$ . In each case, we put down  $N_k = 350$  discretization points on each boundary, and fix the FMM tolerance to be  $10^{-9}$  and the tolerance of the residual to be  $10^{-8}$ .

As is pointed out in Remark 23, the solver consists of a precomputation phase and a solution phase. The CPU time consumed in each phase and the number of interactions are given in Fig. 8. We see that the time per iteration and the time of precomputation have a clean linear growth with respect to the complexity of the boundary, and the number of interactions has a mild growth. The overall complexity is roughly linear.

**Example 3.** In this example, we study the evolution of the effective viscosity over a long time, for which we combine our solver for the quasi-static BVP and the Forward Euler time stepping method for the resulting ODE system as in equation (110).

The initial configuration is chosen to be 25 ellipses with aspect ratios in  $[1, 2]$ , centered on a uniform  $5 \times 5$  grid on the unit square, as is illustrated in Fig. 9. The volume fraction is 0.32. We fix viscosity  $\mu = 1$  and shear rate  $\gamma = 1$ , and discretize each ellipse with 200 points. Solutions of  $\mathbf{u}(\mathbf{x}, t)$  and  $p(\mathbf{x}, t)$  are computed on a  $200 \times 200$  grid on the unit cell, as well as the linear and angular velocities of the ellipses  $\{(\mathbf{v}_i(t), \omega_i(t))\}_{i=1}^{25}$ , and the effective viscosity  $\mu_{\text{eff}}$  at  $t \in [0, 50]$ . Snapshots of

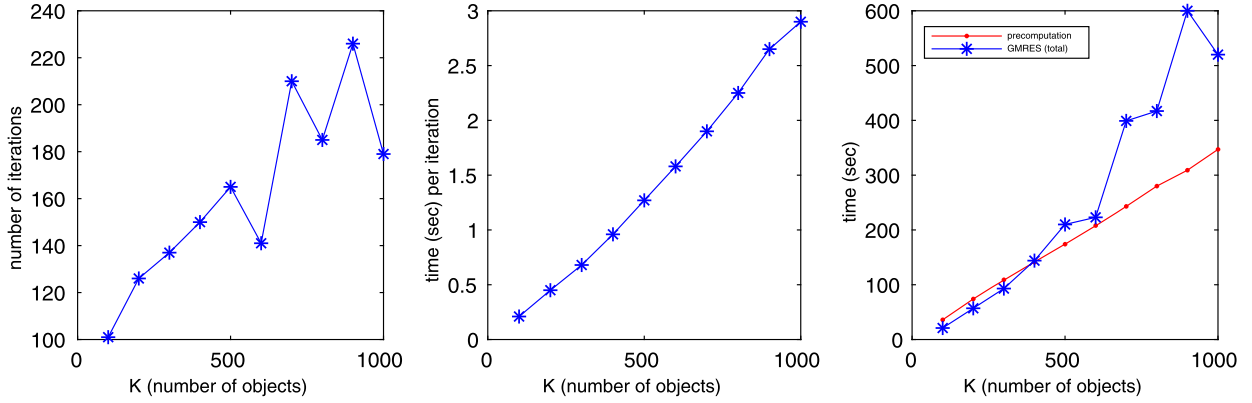


Fig. 8. Scaling of the number of iterations, the CPU time consumed in each iteration, the total GMRES time, and the precomputation time with respect to the complexity of the geometry.

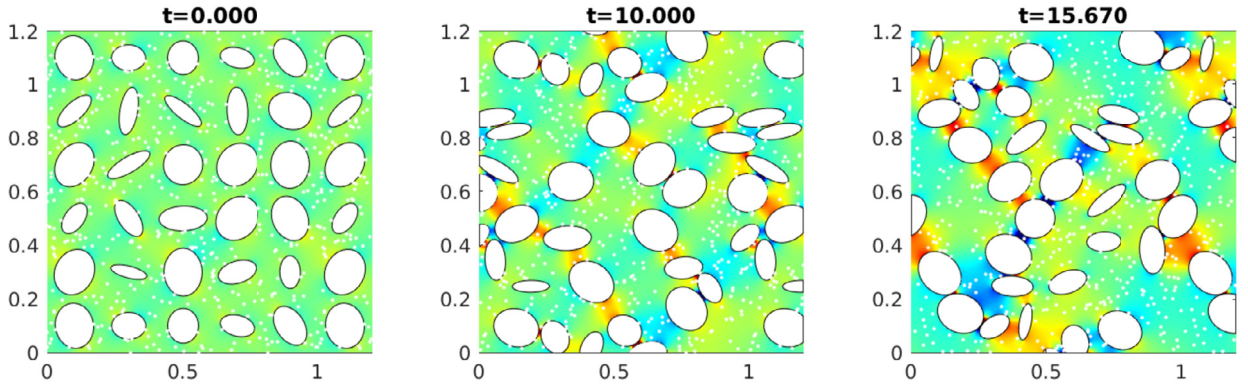


Fig. 9. Snapshots of the solution at different times for 25 ellipses (Example 3). The pressure field is shown in color, and the positions of the boundaries and extra tracer points (white dots) are plotted. The last snapshot is at  $t = 15.67$  where  $\mu_{\text{eff}}(t)$  is very close to a peak (see Fig. 10); note the diagonal force chains (compressional high-pressure lines pointing at around 5 o'clock, extensional lines at around 1 o'clock).

Table 2

Self convergence study of  $\mu_{\text{eff}}(t)$ . Two regimes are tested: at the beginning when  $t \in [0, 1]$ , and when the system enters equilibrium around  $t \in [10, 11]$ . Function values at  $t = 1$  and  $t = 11$  are given, as well as the  $L^2$  error over these time intervals, and the empirical order of convergence. This shows  $\mathcal{O}(\Delta t)$  convergence even at later times, although with an increased prefactor.

$\Delta t$	$\mu(1)$	$\ \mu_{\Delta t} - \mu_{2\Delta t}\ _{L^2([0,1])}$	Order	$\mu(11)$	$\ \mu_{\Delta t} - \mu_{2\Delta t}\ _{L^2([10,11])}$	Order
1.000e-2	1.788484	N/A	N/A	2.345831	N/A	N/A
5.000e-3	1.788799	1.43e-3	N/A	2.336161	7.43e-2	N/A
2.500e-3	1.788956	7.11e-4	1.00	2.331546	5.83e-2	0.35
1.250e-3	1.789035	3.55e-4	1.00	2.329596	3.65e-2	0.68
6.250e-4	1.789074	1.77e-4	1.00	2.328734	2.04e-2	0.84
3.125e-4	1.789093	8.90e-5	0.99	2.328325	1.08e-2	0.92

the solution at different times are shown in Fig. 9, and the effective viscosity is shown in Fig. 10, which suggests that the system has reached a stochastic steady state with diagonal force chains continually forming and breaking up.

We validate the convergence in time by carrying out a self convergence study in  $\mu_{\text{eff}}(t)$  over time intervals  $[0, 1]$  and  $[10, 11]$ . The results are given in Table 2, which shows that first order convergence is always achieved for  $t \in [0, 1]$ , while for  $t \in [10, 11]$ , a much smaller  $\Delta t$  is required for the expected order to be observed. This growth in prefactor in the convergence is to be expected if the ODE system increasingly amplifies deviations in initial conditions with time, for instance if there is a positive Lyapunov exponent.

**Example 4.** We continue the study of the time evolution of the effective viscosity, with a small number of more complicated shapes. In this example, we define the boundary to be a star shape, which, as in Example 2, takes the form  $\mathbf{x}(\theta) = (r(\theta) \cos \theta, r(\theta) \sin \theta)$ , where  $\theta \in [0, 2\pi]$  and  $r(\theta) = 0.25(1 + 0.5 \cos(4\theta))$ . We then place two such stars in the unit square, one centered at  $(0.25, 0.25)$  and the other centered at  $(0.75, 0.75)$ ; see Fig. 11. As in Example 3, we fix the back-

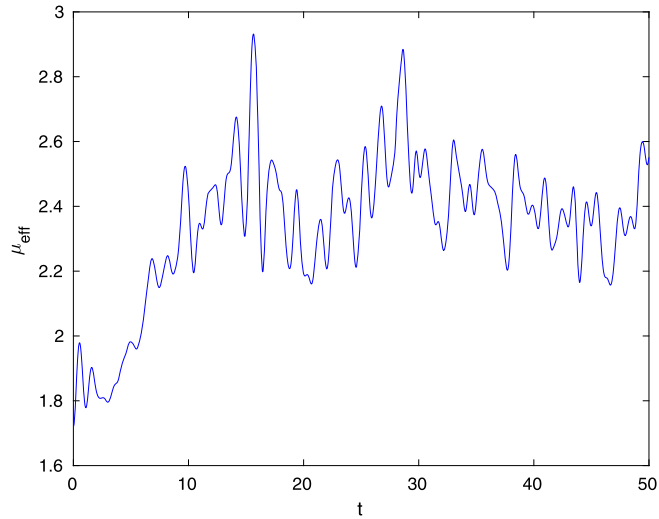


Fig. 10. Time-evolution of the effective viscosity for the 25 ellipses in Example 3.

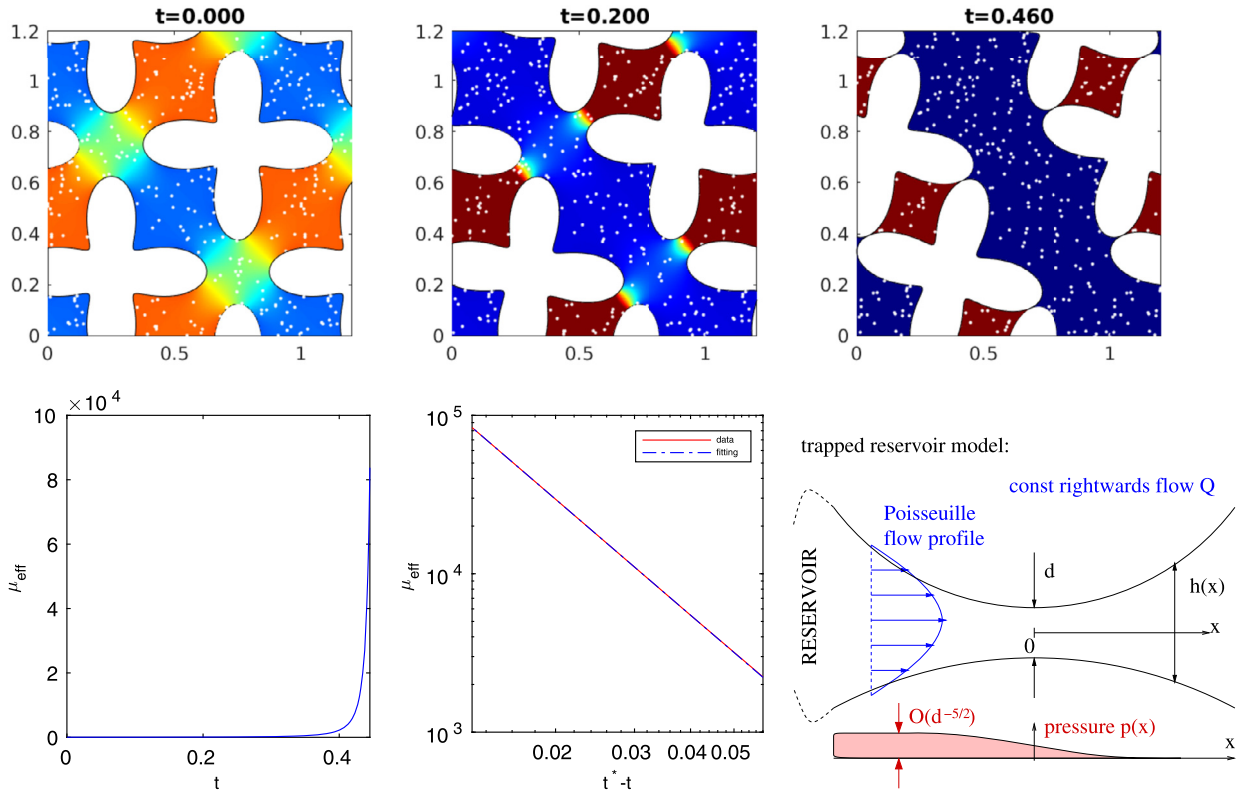
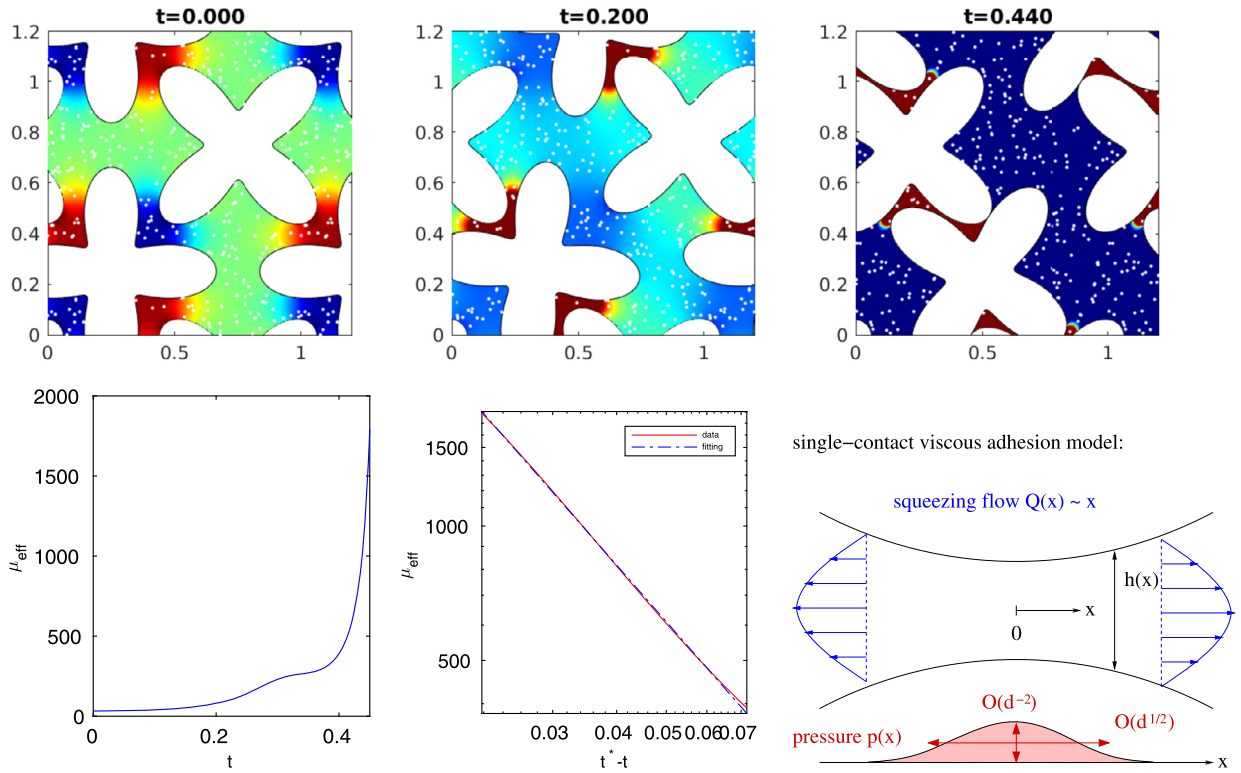


Fig. 11. Jamming with reservoir trapping (Example 4). There are two smooth “star” shaped particles per unit cell. Top row: three snapshots of the evolution, with pressure field in color and tracer points as white dots (times  $t = 0$ ,  $t = 0.2$ ,  $t = 0.46$ ). Bottom left: finite-time blow-up of  $\mu_{\text{eff}}(t)$ . Bottom middle: the best fit (shown on log-log scale) of  $\mu_{\text{eff}}(t)$  to the power-law form (111), giving  $\beta \approx 2.43$ . Bottom right: lubrication theory pipe flow asymptotic model predicting the power  $\beta = 5/2$ .

ground viscosity  $\mu = 1$  and shear rate  $\gamma = 1$ , and use forward Euler as the time stepping method, with  $\Delta t = 5.0e - 4$ . Each boundary is discretized using 2500 points.

Snapshots of the solution and the effective viscosity are shown in Fig. 11. Approaching  $t = 0.46$ ,  $\mu_{\text{eff}}(t)$  grows rapidly without limit, apparently heading towards an infinite value within finite time. This is associated with the geometry becoming “jammed”, i.e., approaching a geometry where the rigid objects themselves prevent further shearing. One might question



**Fig. 12.** Jamming with single point contact (Example 5). There are again two smooth “star” shapes per unit cell, with different parameters from Fig. 11. Top row: three snapshots of the evolution, with pressure field in color and tracer points as white dots (times  $t = 0$ ,  $t = 0.2$ ,  $t = 0.44$ ). Bottom left: finite-time blow-up of  $\mu_{\text{eff}}(t)$ . Bottom middle: the best fit (shown on log-log scale) of  $\mu_{\text{eff}}(t)$  to the power-law form (111), giving  $\beta \approx 1.3$ . Bottom right: lubrication theory viscous adhesion asymptotic model predicting the power  $\beta = 3/2$ .

whether this blow-up is a numerically credible; however, we have tested convergence of the spatial solve and find that errors are below  $10^{-7}$  for  $\mu_{\text{eff}} < 10^5$ , i.e., for all points in the bottom left panel of Fig. 11.

**Remark 26 (Lubrication theory).** It is possible to use a thin-film Stokes model to predict an asymptotic blow-up of the form

$$\mu_{\text{eff}}(t) \sim c|t - t^*|^{-\beta}, \tag{111}$$

where  $t^*$  is the time where objects touch. As Fig. 11 shows, the dominant cause of force is high pressure within a “reservoir” (red) whose volume is contracting approximately linearly in time. The resulting constant flow rate  $Q$  must exit through two narrow channels whose width shrinks like  $d \propto |t - t^*|$ . Taking local coordinates where  $x$  is location along the narrow channel, the Reynolds equation for channel flow [36, Sec. 22.1] is  $\partial p / \partial x = -12Q\mu / h(x)^3$ , where  $h(x)$  is the local width. (See bottom right panel of Fig. 11.) For a smooth curve,  $h(x) = d + cx^2 + O(x^4)$  holds for small  $x$ , so that  $\partial p / \partial x$  is a “bump” function of height  $O(d^{-3})$  and width  $O(d^{1/2})$ . Thus integrating  $p$  on  $(-\infty, \infty)$  gives a pressure drop  $O(d^{-5/2})$ , giving  $\beta = 5/2$  in (111).

We take the values of  $\mu_{\text{eff}}(t)$  for  $t \in [0.4, 0.44]$ , where the spatial solve is accurate and  $\mu_{\text{eff}}(t)$  is in an asymptotic regime, and apply nonlinear least squares to fit the parameters  $c$ ,  $t^*$  and  $\beta$ . The results are  $c = 2.187$ ,  $t^* = 0.458$  and  $\beta = 2.431$ , with a relative residual of 0.0004 and excellent agreement visible in Fig. 11. The  $\beta$  value is thus very close to the predicted 2.5.

**Remark 27 (Single-contact jamming).** The  $\mu_{\text{eff}}$  blow-up observed above relied on a reservoir trapped by two contact points. Another type of jamming is possible, with a single approaching contact point between two smooth surfaces. This situation is known as viscous adhesion [36, Sec. 22.5]. By contrast, now the flow depends on location,  $Q(x) \propto x$ , and a similar asymptotic analysis as above gives a pressure peak of  $O(d^{-2})$ , width  $O(d^{1/2})$ , thus the weaker power  $\beta = 3/2$ . (See bottom right panel of Fig. 12.)

**Example 5.** An initial configuration giving single-contact jamming is as follows. The two star shapes are  $\mathbf{x}(\theta) = (r(\theta)\cos\theta, r(\theta)\sin\theta)$ , where  $\theta \in [0, 2\pi]$  and  $r(\theta) = 0.275(1 + 0.5\cos(4\theta))$ . We then shift them so that the first one is

centered at (0.25, 0.25) and the second at (0.75, 0.75). The second star is then rotated counter-clockwise by  $\pi/4$ . We keep other parameters unchanged and run the same simulation.

As Fig. 12 shows, jamming is observed for  $t \approx 0.47$ . We take the values of  $\mu_{\text{eff}}(t)$  for  $t \in [0.4, 0.45]$ , and as before fit the parameters in (111), getting  $c = 12.16$ ,  $t^* = 0.472$ , and  $\beta = 1.31$ , with a relative residual of 0.006. Thus the power law does not match the predicted  $\beta = 1.5$  as well as in Example 4, but is still quite close.

### 9. Conclusion

We have developed an integral equation based fast solver for the highly accurate simulation of a doubly-periodic suspension of arbitrary smooth rigid particles in a shearing Stokes flow. The effort per time-step scales linearly in the complexity of the geometry. Our method combines a general framework for periodization which is robust and flexible, a Stokes FMM, and a special quadrature rule for close to boundary targets. The latter gives spectral accuracy in the spatial (quasi-static) solve. With reasonable sampling of each particle's boundary, our method proves to be accurate even for particles separated by distances as close as  $10^{-4}$  times the particle size. A first order explicit Euler method is adopted for time stepping, although our formulation easily allows higher order time stepping. The solver models pure hydrodynamic interactions without artificial repulsion between particles; we have found that, at least for ellipses at moderate volume fractions, that accurate spatial solutions and small time steps mean that no collisions occur even after tens of shear times. With more complex shapes chosen so that collisions occur in finite time, we demonstrate that a lubrication theory model correctly predicts the numerical asymptotic power-law force blow-up.

The solver presented could find application in studying complex nonlinear rheology, the shape and volume fraction dependence of effective viscosity, and transport/mixing statistics. It can trivially be generalized to time-varying shear rate to study hysteretic or finite-frequency shear oscillation effects. It is also easy to include gravitational forces to study sedimentation.

There are several challenges that we plan to address in future work. For guaranteed accuracy in the spatial solve at closer distances, adaptivity (e.g. using panel-based discretization of the boundaries) would be needed [35,45]. Higher-order time-stepping is essential to exploit, but it remains an issue to handle the apparent stiffness when two or more particles come close to each other [31]. At higher volume fractions it appears that one cannot avoid including artificial repulsions or collision-avoidance [29,47]. The generalization to three dimensions is relatively straightforward, via high-order surface quadratures, or schemes for spheres [47], and will be reported at a later date.

### CRedit authorship contribution statement

**Jun Wang:** Methodology, Software, Visualization, Writing - original draft. **Ehssan Nazockdast:** Conceptualization, Validation, Writing - review & editing. **Alex Barnett:** Conceptualization, Methodology, Visualization, Writing - review & editing.

### Declaration of competing interest

The authors declare that they have no known competing financial interests or personal relationships that could have appeared to influence the work reported in this paper.

### Acknowledgements

We are grateful for discussions with Manas Rachh, Charlie Epstein, Mike Shelley, and Leslie Greengard, and the input of the anonymous referees. The Flatiron Institute is a division of the Simons Foundation.

### Appendix A. Proof of Theorem 9

We are given a smooth pair  $(\mathbf{w}, r)$  which generates the discrepancy  $\mathbf{g}$  via (44)–(47). We wish to prove existence of  $(\mathbf{v}, q)$  solving the EBVP (38)–(43). Let  $\mathbf{h} := \mu \Delta \mathbf{w} - \nabla r \in (C^\infty(\overline{\mathcal{U}}))^2$  and  $h := -\nabla \cdot \mathbf{w} \in C^\infty(\overline{\mathcal{U}})$ . Now associate  $\mathcal{U}$  with the flat torus  $\mathbb{T}^2$  with the same lattice vectors, and notice that  $\mathbf{h}$  and  $h$ , as functions on  $\mathbb{T}^2$ , are generally discontinuous but bounded, hence in  $L^2(\mathbb{T}^2)$ . Then let  $(\mathbf{u}, p)$  be a periodic solution pair to the inhomogeneous Stokes BVP on  $\mathbb{T}^2$ :

$$-\mu \Delta \mathbf{u} + \nabla p = \mathbf{h} \quad \text{in } \mathbb{T}^2 \tag{A.1}$$

$$\nabla \cdot \mathbf{u} = h \quad \text{in } \mathbb{T}^2. \tag{A.2}$$

Recall that the Stokes system is elliptic in the Douglis–Nirenberg sense (see, e.g., [42, Sec. 2.2.2]). The manifold  $\mathbb{T}^2$  has no boundary, so ellipticity implies that the Stokes operator in this domain is Fredholm (e.g. [44, Theorem 8.53]). It is also self-adjoint. Thus if  $(\mathbf{h}, h)$  is orthogonal to the nullspace, a solution to (A.1)–(A.2) exists. That the nullspace is precisely the span of the constant functions, hence is 3-dimensional, is a simple result proven in [2, Prop. 4.2]. Thus we need only show that  $\mathbf{h}$  and  $h$  defined above integrate to zero. We compute, using the divergence theorem for Stokes (69),

$$\int_{\mathcal{U}} \mathbf{h} = \int_{\mathcal{U}} (\mu \Delta \mathbf{w} - \nabla r) = \int_{\partial \mathcal{U}} \mathbf{T}(\mathbf{w}, r) = \int_L \mathbf{g}_2 + \int_D \mathbf{g}_4 = \mathbf{0},$$

by the consistency condition (48) on  $\mathbf{g}$ . Similarly, using the usual divergence theorem,

$$\int_{\mathcal{U}} h = - \int_{\mathcal{U}} \nabla \cdot \mathbf{w} = - \int_{\partial \mathcal{U}} \mathbf{n} \cdot \mathbf{w} = - \int_L \mathbf{n} \cdot \mathbf{g}_1 - \int_D \mathbf{n} \cdot \mathbf{g}_3 = 0,$$

by (49). Thus,  $(\mathbf{u}, p)$  exists. Finally, let  $\mathbf{v} = \mathbf{w} + \mathbf{u}$ , and  $q = r + p$ . Since the volume right-hand side terms cancel, it is easy to check that  $(\mathbf{v}, q)$  satisfies the EBVP (38)–(43).

By ellipticity of the Stokes system, since the driving  $(\mathbf{h}, h)$  is  $C^\infty$  in the interior  $\mathcal{U}$ , the same is true for the solution  $(\mathbf{u}, p)$ , and hence, by smoothness of  $(\mathbf{w}, r)$ , also for  $(\mathbf{v}, q)$ .  $\square$

### Appendix B. Proof of Theorem 12

We first show that  $\mathbf{g}$  is consistent in the sense of (48)–(49).

$$\begin{aligned} \int_L \mathbf{g}_2 ds + \int_D \mathbf{g}_4 ds &= \int_L (-T_R^{near} + T_L^{near} + \frac{\mathbf{f}}{2|\mathbf{e}_2|}) ds + \int_D (-T_U^{near} + T_D^{near} + \frac{\mathbf{f}}{2|\mathbf{e}_1|}) ds \\ &= \frac{\mathbf{f}}{2|\mathbf{e}_2|} \int_L ds + \frac{\mathbf{f}}{2|\mathbf{e}_1|} \int_D ds + \int_{\partial \mathcal{U}} T^{near} ds \\ &= \mathbf{f} - \mathbf{f} = \mathbf{0}. \\ \int_L \mathbf{g}_1 \cdot \mathbf{n} ds + \int_D \mathbf{g}_3 \cdot \mathbf{n} ds &= \int_L (\mathbf{w}_L^{near} - \mathbf{w}_R^{near}) \cdot \mathbf{n} ds + \int_D (\mathbf{w}_D^{near} - \mathbf{w}_U^{near}) \cdot \mathbf{n} ds \\ &= \int_{\partial \mathcal{U}} \mathbf{w}^{near} \cdot ds = \int_{\partial \mathcal{U}} \mathbf{w} \cdot \mathbf{n} ds = 0. \end{aligned}$$

We must now show that there is a  $(\mathbf{w}, q)$  which generates the  $\mathbf{g}$  given in (52)–(55). Since  $\mathbf{y}$  is in the open set  $\mathcal{U}$ , thus a nonzero distance from  $\partial \mathcal{U}$ , there exists a mollifier  $\psi \in C^\infty(\bar{\mathcal{U}})$  which is identically 1 in a neighborhood of  $\partial \mathcal{U}$  but identically zero in a neighborhood of  $\mathbf{y}$ . Then the smooth functions  $\mathbf{w} = \psi \mathbf{w}^{near}$  and  $q = \psi q^{near}$  generate (in the sense of Theorem 9) the bracketed terms in (52)–(55). Smooth functions may then be added to  $\mathbf{w}$  to generate the additional  $\mathbf{f}$ -dependent constant terms in  $\mathbf{g}_2$  and  $\mathbf{g}_4$ . To see this, for example, when the unit cell has height 1, one may check using  $\mathbf{n}_1 = (0, 1)$  that the smooth vector function  $\mathbf{w}(x_1, x_2) = (f_1/2, f_2/4)x_2^2/\mu|\mathbf{e}_1|$ , and  $q \equiv 0$ , generates  $\mathbf{g}_4 = \mathbf{f}/2|\mathbf{e}_1|$  as needed in (55). The term needed in  $\mathbf{g}_2$  may be similarly generated by rotating a similar function. Thus there is a  $(\mathbf{w}, q)$  in  $C^\infty(\bar{\mathcal{U}})$  generating  $\mathbf{g}$ . Finally, we apply Theorem 9.  $\square$

### References

- [1] L. af Klinteberg, A.-K. Tornberg, Fast Ewald summation for Stokesian particle suspensions, *Int. J. Numer. Methods Fluids* 76 (2014) 669–698.
- [2] A.H. Barnett, G. Marple, S. Veerapaneni, L. Zhao, A unified integral equation scheme for doubly-periodic Laplace and Stokes boundary value problems in two dimensions, *Commun. Pure Appl. Math.* 71 (11) (2018) 2334–2380.
- [3] A.H. Barnett, B. Wu, S. Veerapaneni, Spectrally-accurate quadratures for evaluation of layer potentials close to the boundary for the 2D Stokes and Laplace equations, *SIAM J. Sci. Comput.* 37 (4) (2015) B519–B542.
- [4] A.H. Barnett, B. Wu, S. Veerapaneni, Spectrally-accurate quadratures for evaluation of layer potentials close to the boundary for the 2d Stokes and Laplace equations, *SIAM J. Sci. Comput.* 37 (4) (2015) B519–B542.
- [5] J. Bender, N.J. Wagner, Reversible shear thickening in monodisperse and bidisperse colloidal dispersions, *J. Rheol.* 40 (5) (1998) 899.
- [6] L.V. Berlyand, Y. Gorb, A. Novikov, Fictitious fluid approach and anomalous blow-up of the dissipation rate in a two-dimensional model of concentrated suspensions, *Arch. Ration. Mech. Anal.* 193 (3) (7 2009) 585–622.
- [7] J.F. Brady, G. Bossis, Stokesian dynamics, *Annu. Rev. Fluid Mech.* 20 (1) (1988) 111–157.
- [8] J.F. Brady, J.F. Morris, Microstructure of strongly sheared suspensions and its impact on rheology and diffusion, *J. Fluid Mech.* 348 (1997) 103–139.
- [9] X. Cheng, J.H. McCoy, J.N. Israelachvili, I. Cohen, Imaging the microscopic structure of shear thinning and thickening colloidal suspensions, *Science* 333 (6047) (2011) 1276–1279.
- [10] E. Corona, L. Greengard, M. Rachh, S. Veerapaneni, An integral equation formulation for rigid bodies in Stokes flow in three dimensions, *J. Comput. Phys.* 332 (2017) 504–519.
- [11] C.D. Cwalina, K.J. Harrison, N.J. Wagner, Rheology of cubic particles suspended in a Newtonian fluid, *Soft Matter* 12 (20) (2016) 4654–4665.
- [12] L. Durlafsky, J.F. Brady, G. Bossis, Dynamic simulation of hydrodynamically interacting particles, *J. Fluid Mech.* 180 (1987) 21–49.
- [13] R.G. Egres, N.J. Wagner, The rheology and microstructure of acicular precipitated calcium carbonate colloidal suspensions through the shear thickening transition, *J. Rheol.* 49 (3) (2005) 719–746.
- [14] G.B. Folland, *Introduction to Partial Differential Equations*, second edition, Princeton University Press, 1996.
- [15] D.R. Foss, J.F. Brady, Structure, diffusion and rheology of Brownian suspensions by Stokesian Dynamics simulation, *J. Fluid Mech.* 407 (2000) 167–200.
- [16] F. Gadala-Maria, A. Acrivos, Shear-induced structure in a concentrated suspension of solid spheres, *J. Rheol.* 24 (6) (1980) 799–814.

- [17] L. Greengard, M.C. Kropinski, Integral equation methods for Stokes flow in doubly-periodic domains, *J. Eng. Math.* 48 (2004) 157–170.
- [18] L. Greengard, V. Rokhlin, A fast algorithm for particle simulations, *J. Comput. Phys.* 73 (1987) 325–348.
- [19] E. Guazzelli, J.F. Morris, *A Physical Introduction to Suspension Dynamics*, vol. 45, Cambridge University Press, 2011.
- [20] A.K. Gurnon, N.J. Wagner, Microstructure and rheology relationships for shear thickening colloidal dispersions, *J. Fluid Mech.* 769 (2015) 242–276.
- [21] J.J. Haan, P.S. Steif, Particle-phase pressure in a slow shearing flow based on the numerical simulation of a planar suspension of rough contacting cylinders, *J. Rheol.* 42 (1998) 891–916.
- [22] J. Helsing, R. Ojala, On the evaluation of layer potentials close to their sources, *J. Comput. Phys.* 227 (2008) 2899–2921.
- [23] G. Hsiao, W.L. Wendland, *Boundary Integral Equations, Applied Mathematical Sciences*, vol. 164, Springer, 2008.
- [24] L.C. Hsiao, S. Jamali, E. Glynos, P.F. Green, R.G. Larson, M.J. Solomon, Rheological state diagrams for rough colloids in shear flow, *Phys. Rev. Lett.* 119 (15) (2017) 158001.
- [25] S. Jamali, J.F. Brady, Alternative frictional model for discontinuous shear thickening of dense suspensions: hydrodynamics, *Phys. Rev. Lett.* 123 (13) (2019) 138002.
- [26] S.J. Karrila, S. Kim, Integral equations of the second kind for Stokes flow: direction solution for physical variables and removal of inherent accuracy limitations, *Chem. Eng. Commun.* 82 (1) (1989) 123–161.
- [27] O.D. Kellogg, *Foundations of Potential Theory*, first edition, Springer-Verlag, Berlin, Heidelberg, 1967.
- [28] R.E. Larson, J.J.L. Higdon, Microscopic flow near the surface of two-dimensional porous media. Part 2. Transverse flow, *J. Fluid Mech.* 178 (1987) 119–136.
- [29] L. Lu, A. Rahimian, D. Zorin, Contact-aware simulations of particulate Stokesian suspensions, *J. Comput. Phys.* 347 (2017) 160–182.
- [30] B.J. Maranzano, N.J. Wagner, The effects of particle size on reversible shear thickening of concentrated colloidal dispersions, *J. Chem. Phys.* 114 (23) (2001) 10514–10527.
- [31] J. Melrose, R. Ball, The pathological behaviour of sheared hard spheres with hydrodynamic interactions, *Europhys. Lett.* 32 (6) (1995) 535.
- [32] J. Mewis, N.J. Wagner, *Colloidal Suspension Rheology*, Cambridge University Press, 2012.
- [33] E. Nazockdast, J.F. Morris, Microstructural theory and the rheology of concentrated colloidal suspensions, *J. Fluid Mech.* 713 (2012) 420–452.
- [34] K.C. Nunan, J.B. Keller, Effective viscosity of a periodic suspension, *J. Fluid Mech.* 142 (1984) 269–287.
- [35] R. Ojala, A.-K. Tornberg, An accurate integral equation method for simulating multi-phase Stokes flow, *J. Comput. Phys.* 298 (2015) 145–160.
- [36] R.L. Panton, *Incompressible Flow*, fourth edition, Wiley, 2013.
- [37] M. Rachh, L. Greengard, Integral equation methods for elastance and mobility problems in two dimensions, arXiv:1507.05925, 2015.
- [38] M. Rachh, L. Greengard, Integral equation methods for elastance and mobility problems in two dimensions, *SIAM J. Numer. Anal.* 54 (5) (2016) 2889–2909.
- [39] A.S. Sangani, G. Mo, Inclusion of lubrication forces in dynamic simulations, *Phys. Fluids* 6 (5) (1994) 1653–1662.
- [40] A. Sierou, J.F. Brady, Accelerated stokesian dynamics simulations, *J. Fluid Mech.* 448 (2001) 115–146.
- [41] M. Souzy, X. Yin, E. Villermaux, C. Abid, B. Metzger, Super-diffusion in sheared suspensions, *Phys. Fluids* 27 (2015) 041705.
- [42] V. Volpert, *Elliptic Partial Differential Equations. Volume 1: Fredholm Theory of Elliptic Problems in Unbounded Domains*, Birkhäuser, Springer Basel, 2011.
- [43] M. Wang, J.F. Brady, Spectral Ewald acceleration of stokesian dynamics for polydisperse suspensions, *J. Comput. Phys.* 306 (2016) 443–477.
- [44] J.T. Wloka, B. Rowley, B. Lawruk, *Boundary Value Problems for Elliptic Systems*, Cambridge University Press, 1995.
- [45] B. Wu, H. Zhu, A.H. Barnett, S. Veerapaneni, Solution of Stokes flow in complex nonsmooth 2D geometries via a linear-scaling high-order adaptive integral equation scheme, preprint, arXiv:1909.00049 [math.NA], 2019.
- [46] B. Xu, J.F. Gilchrist, Microstructure of sheared monosized colloidal suspensions resulting from hydrodynamic and electrostatic interactions, *J. Chem. Phys.* 140 (20) (2014) 204903.
- [47] W. Yan, E. Corona, D. Malhotra, S. Veerapaneni, M. Shelley, A scalable computational platform for particulate Stokes suspensions, *J. Comput. Phys.* 416 (2020) 109524.